Journal of Solid State Electrochemistry
https://doi.org/10.1007/s10008-025-06475-y

REVIEW PAPER

In-situ Raman spectroscopy studies of solid oxide electrochemical devices: a review

Dmitrii A. Agarkov[1]

Received: 10 October 2025 / Revised: 31 October 2025 / Accepted: 1 November 2025

Abstract

This survey focuses on in-situ studies of solid oxide fuel cells (SOFCs) and other solid oxide electrolyte devices using Raman spectroscopy, which is often combined with other electrochemical and physical methods. Most conventional techniques, for example, structural and microscopy techniques and methods of elemental analysis, cannot provide an opportunity to conduct in-situ analysis of the processes that occur in the materials, electrodes, and entire SOFCs due to high operating temperatures (up to 850–900 °C), high current densities (often up to the level of several A/cm^2), aggressive gas environments, and separated cathode and anode gas chambers. Conventional electrochemical techniques cannot provide the local information. On the contrary, Raman spectroscopy enables remote, noninvasive, local and molecular-sensitive testing of SOFCs, thus making it possible to obtain information on the macro- and microscopic mechanisms and to perform targeted optimization of the composition, microstructure, and operating conditions of SOFC components. This review aims to cover recent research focused on separate SOFC materials, electrochemical half-cells, and full SOFCs. Special attention is given to carbon deposition at SOFC anodes fueled with hydrocarbon-containing mixtures, mechanisms of hydrocarbon electrooxidation, anode reduction kinetics, poisoning with S- and Cl-containing impurities, variations in oxygen chemical potential, and assessment of emerging mechanical stresses.

Keywords Raman spectroscopy · In-situ analysis · Solid oxide fuel cells · Carbon deposition · Sulfur poisoning · Mechanical stress · Oxygen chemical potential · Gas analysis

Abbreviations

3YSZ	Zirconium dioxide stabilized with 3 mol.% yttrium oxide
8YSZ	Zirconium dioxide stabilized with 8 mol.% yttrium oxide
10Sc1YSZ	Zirconium dioxide stabilized with 10 mol.% scandium oxide and 1 mol.% yttrium oxide
10Sc1CeSZ	Zirconium dioxide stabilized with 10 mol.% scandium oxide and 1 mol.% cerium oxide
20SDC	Cerium dioxide doped with 20 mol.% scandium oxide
ACC	Anode current-collecting layer
AF	Anode functional layer
ASC	Anode-supported cell
BZCYYb	$BaZr_{0.1}Ce_{0.7}Y_{0.1}Yb_{0.1}O_{3-d}$
DFT	Density functional theory
DIR	Direct internal reforming
EDX	Energy-dispersive X-ray spectroscopy
ESC	Electrolyte-supported cell
FTIR	Fourier transform infrared spectroscopy
FE-SEM	Field emission scanning electron microscopy
FIB	Focused ion beam
GDC	Cerium dioxide doped with gadolinium oxide
IR	Infrared
IS	Impedance spectroscopy
LSCF	Lanthanum strontium cobaltite ferrite $(La, Sr)_x(Co, Fe)_{1-x}O_{3-d}$
NIR	Near-infrared spectroscopy
OCP	Open circuit potential
OCV	Open circuit voltage
Ppm	Parts per million
RS	Raman spectroscopy

✉ Dmitrii A. Agarkov
agarkov@issp.ac.ru

[1] Osipyan Institute of Solid State Physics RAS, Chernogolovka, Russia

Published online: 06 December 2025

SDC	Cerium dioxide doped with samarium oxide
SEM	Scanning electron microscopy
SERS	Surface-enhanced Raman spectroscopy
SOFC	Solid oxide fuel cell
SOEC	Solid oxide electrolysis cell
STN	Niobium-doped strontium titanate
SZY	$SrZr_{0.95}Y_{0.05}O_{3-d}$
TEM	Transmission electron microscope
TPB	Triple phase boundary
WGSR	Water–gas shift reaction
XRD	X-ray diffractionYSZ
YSZ	Zirconium dioxide stabilized with yttrium oxide

Introduction

Over the past two or three decades, solid oxide fuel cells (SOFCs), stacks, and power plants based on them have attracted great interest from researchers and developers in many developed and developing countries [1–3]. SOFCs are electrochemical devices that directly convert the chemical energy of oxidation of hydrogen or gaseous hydrocarbons into electrical energy and high-potential thermal energy with a record high efficiency. The electrical energy efficiency is often 45–60% [4, 5] but can exceed 60% for some systems, particularly hybrid systems with gas turbines [6]. The total efficiency of electrical and used thermal energy often exceeds 85–90% [6, 7]. Other important advantages of SOFC-based power systems include the following features: a long service interval of about a year with short and simple technical maintenance, i.e. replacement of the desulfurization cartridge; long service life of 40,000–50,000 h, there are large-scale research and development programs aimed at increasing the service life to 100,000 h [8]; multi-fuel, i.e. the ability to use hydrogen and a wide range of gaseous hydrocarbons as fuel, such as methane, propane, butane, dimethyl ether, dimethoxymethane, bioethanol, biogas, landfill gases [9, 10], wastewater gases, gasified diesel fuel [11], and other types of fuel; high environmental friendliness: CO and NO_x emissions are hundreds of times lower than the values specified in the Euro 6 and Tier 4 environmental standards [12].

The operating principle of a SOFC is as follows. A single solid oxide fuel cell – a membrane-electrode assembly – consists of a solid electrolyte membrane with oxygen anion conductivity (O^{2-}), as well as a cathode and an anode located on opposite sides of the membrane. Air is supplied to the SOFC cathode, and, due to the catalytic properties of the cathode material, molecular oxygen (O_2) dissociates to anions (O^{2-}). The anions then move through the solid electrolyte membrane to the anode due to anion conductivity. Syngas, which is a mixture of hydrogen (H_2) and carbon monoxide (CO), is supplied to the anode. The mixture is prepared in an external device – a fuel processor [13] – or directly at the anode. This approach is called "internal reforming" [14]. Oxygen anions from the solid electrolyte membrane oxidize hydrogen (H_2) to water (H_2O) and carbon monoxide (CO) to carbon dioxide (CO_2). The electrons required for the dissociation of molecular oxygen at the cathode and subsequent oxidation of the fuel at the anode pass through an external electric circuit, thus performing useful work. Depending on the design and functional materials used, the operating temperature of the SOFC is 400–900 °C [3, 15], which allows for the production of high-potential heat in the form of hot water vapor (anode reaction product) or hot air used for the thermal regulation of the system.

The main efforts of SOFC researchers and developers are focused on reducing the total internal resistance of SOFCs [16] in order to minimize losses of chemical energy from fuel oxidation during their operation. The total internal resistance is determined by the ohmic resistance of the components (electrolyte, cathode and anode) and the polarization resistance corresponding to the electrode current-generating processes (cathodic and anodic) [17, 18].Targeted optimization of the polarization resistance of SOFCs is impossible without understanding the micromechanisms of current-generating processes. Direct in-situ studies of these processes are significantly hampered by the specific operating conditions of the system: operating temperature at the level of 500–900 °C [19, 20], separated fuel and oxidizing gas volumes, and aggressive gas environments. One of the most promising methods for in-situ studies of the mechanisms of electrode processes in SOFCs, including various types of cathode and anode separation, carbon deposition, mechanical stresses, and other physicochemical processes, is Raman spectroscopy [21]. This method is molecular-sensitive [22], non-invasive [23], non-destructive [24], and remote. An extremely extensive, comprehensive database of spectra of various materials used in SOFC fabrication has been accumulated over more than 90 years of research [25]. This paper reviews scientific articles in which Raman scattering was used to study the following aspects of SOFCs: mechanical stresses, carbon deposition on anodes, sulfur and chlorine poisoning, kinetics of anode reduction, and evolution of oxygen chemical potential.

Figure 1 illustrates the number of articles found in the Google Scholar indexing system for scientific publications [26] for the queries "raman", "sofc", and "raman" "sofc" normalized to values for 2023.

The figure shows that the number of articles for the query "raman" (black circles) passed its peak value around 2017–2018. The peak exceeded 250% of the number of publications for 2023 and is followed by a fairly confident decline

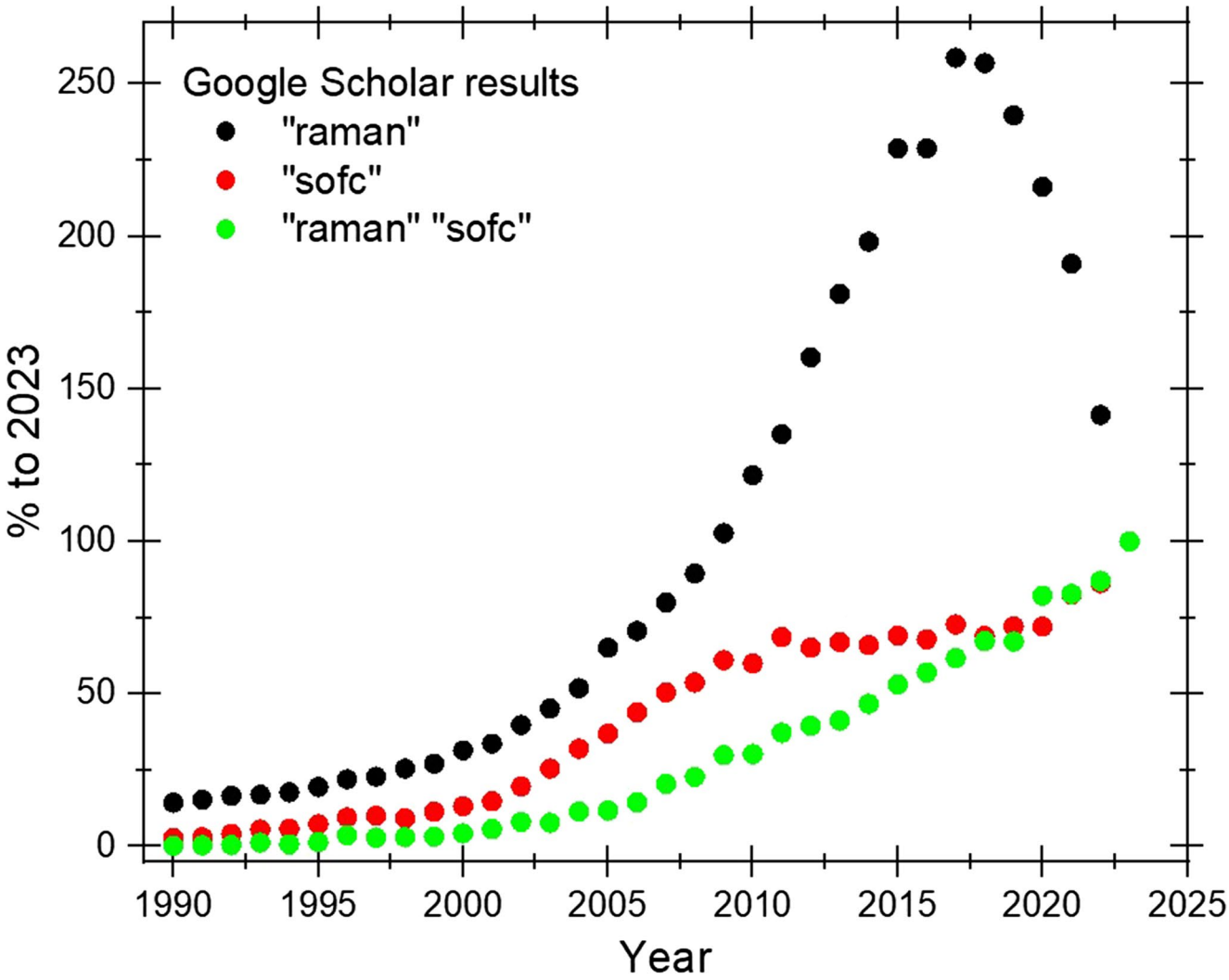

Fig. 1 The number of scientific articles for the queries "raman", "sofc", and "raman" "sofc" in the Google Scholar indexing system of scientific publications normalized to values for 2023

that continues to this day. It should be emphasized that this decline occurs despite the constant growth in the number of scientific publications in the world by 4–8% per year [27–29]. The result indicates a decrease in scientific interest in Raman spectroscopy, which is probably due to a long history of research.

The number of publications for the query "sofc" (red circles) increases throughout the graph; however, there is a noticeable slowdown starting around 2010. This behavior can be easily explained by the entry of a number of stacks [30, 31] and SOFC power plants [32, 33] into the market, indicating an increase in the level of technology readiness. Note that the graph of the dependence of the number of publications for the query "raman" "sofc" (green circles) normalized for 2023 shows a steady and accelerating growth (the curve is convex downwards), indicating an increase in interest in SOFC research using Raman spectroscopy.

Figure 2 presents a schematic illustration of typical approaches for studies of solid oxide electrochemical devices employing in-situ Raman spectroscopy.

A solid oxide fuel or an electrolysis cell is often placed in a system that enables the maintenance and/or variation of the operating conditions as necessary. The cell is exposed to exciting laser light, and the scattered radiation is collected for Raman analysis. This analysis is often combined with other methods, including electrochemical tests (e.g., study of current-voltage characteristics, impedance spectra, etc.) and gas analysis.

Analysis of mechanical stresses in SOFCs

The study of mechanical stresses arising in operating SOFCs is crucial for optimizing their service life characteristics, as well as predicting and mitigating factors that significantly

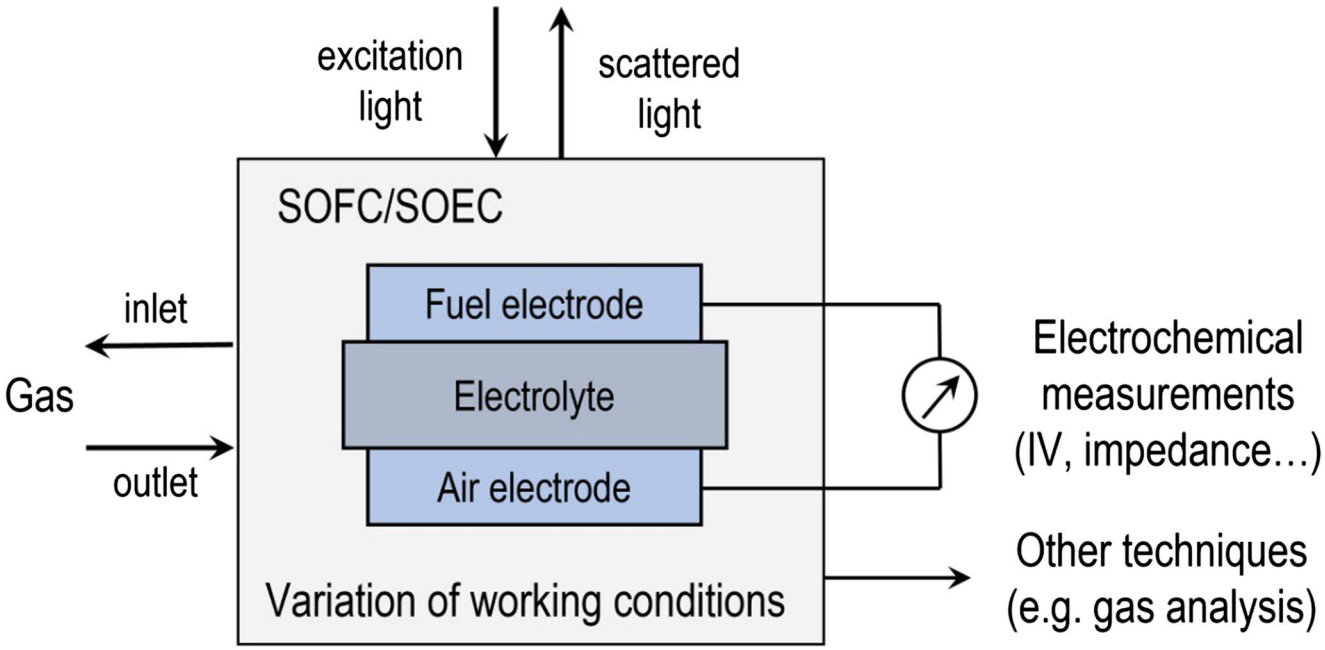

Fig. 2 Schematic illustration of typical approaches for conducting in-situ Raman spectroscopy studies of solid oxide electrolyte devices

Table 1 A summary of the reports where studies of mechanical stresses in SOFCs were carried out using Raman spectroscopy

Cells and materials	Studied RS line	Brief conclusion	Ref.
SOFC: Ni-8YSZ/8YSZ/20SDC/LSCF	F_{2g} SDC	The stress conditions in the electrolyte before operation were estimated to be compressive, which is consistent with the X-ray diffraction data. During operation, the stress conditions changed to tensile due to the reduction of NiO to Ni.	[37]
GDC and SDC powders	F_{2g} GDC F_{2g} SDC	The Raman detection system with an accuracy of 0.1 cm^{-1} could recognize differences in stress conditions within the sublayer with an accuracy of 40–50 MPa.	[38]
]SOFC: Ni-8YSZ/8YSZ/20SDC/LSCF	F_{2g} SDC	The technique can be easily applied to model SOFCs and provides quantitative information on mechanical stresses in the electrolyte, taking into account Sm concentration and temperature.	[39]
SOFC: Ni-8YSZ/8YSZ/20SDC/LSCF with a removed cathode	F_{2g} SDC	The dopant concentration varied depending on the thermal cycles, and Sm probably diffused from the intermediate layer into the electrolyte.	[40]
SOFC: Ni-8YSZ/8YSZ/20SDC/LSCF	F_{2g} SDC	In-situ Raman spectroscopy showed its applicability for assessing mechanical stresses in different functional layers of cells with an anode substrate and a dense sublayer.	[41]

affect the failure of such electrochemical devices [34–36]. In many works, in-situ Raman spectroscopy is used to study mechanical stresses arising under SOFC operating conditions. A summary of such studies is provided in Table 1.

The prospects of the method for studying mechanical stresses were correctly predicted in the review paper [42]. Ref. [37] can be considered the pioneering experimental work in this field. Stresses in a complete and functioning SOFC with a Ni-8YSZ/8YSZ/20SDC/LSCF layer composition were studied. Changes in the residual stress were estimated during the oxidation-reduction cycle at a chemical potential gradient and an operating temperature of 800 °C. As a result, the stress conditions in the electrolyte before operation were estimated to be compressive, which is consistent with the X-ray diffraction data. During operation, the stress conditions changed due to the reduction of NiO to Ni. Compressive stress changed to tensile stress. In

addition, the standard deviation of stress became greater than before reoxidation and was irreversible.

In Ref. [38], individual materials were first studied at high pressure. Then, the resulting calibration was considered for application to a functioning SOFC. Obtained relationship showed that the Raman peak in the SOFC sublayer with an anode substrate shifted by approximately 2 cm^{-1} when the in-plane stress changed by 1 GPa. Therefore, a Raman detection system with an accuracy of 0.1 cm^{-1} could recognize differences in stress conditions within the sublayer with an accuracy of 40–50 MPa. In subsequent work by this team, the developed technique was applied to functioning SOFCs in-situ.

The concentration of Sm in the sublayer of model cells was determined. Using this value as a reference, the half-width of the F_{2g} peak was used as a temperature index after heating the model cell [39]. The position of the F_{2g} peak for SDC without mechanical stress at different temperatures and Sm concentrations was also obtained. These results improved the estimation of the stress state to evaluate not only the stress state but also the dopant concentration and temperature with high spatial resolution.

In another work by the same authors [40], not only was the half-width of the F_{2g} peak used for the study, but the change in its position was also considered. During the test, two thermal cycles were used, which simulated the start and stop of the SOFC operation. The concentration of the dopant changed depending on the thermal cycles; samarium might diffuse from the intermediate layer into the electrolyte.

In a much later work [41], similar cells were examined using in-situ Raman spectroscopy, and the same Raman peak was employed to study the mechanical stresses. The mechanical stresses in different functional layers of the SOFC were estimated: the anode, electrolyte, sublayer, and cathode. The results showed that the method was not suitable for cells with a porous sublayer since the stress conditions differed from the in-plane stress conditions assumed by the method. In contrast, the results for cells with a dense sublayer showed that the stress conditions were accurately estimated over the range from room temperature to operating temperatures. Therefore, in-situ Raman spectroscopy was demonstrated to be applicable for estimating mechanical stresses in different functional layers of cells with an anode substrate and a dense sublayer.

In [43], a comparison was made between the measurements of residual stress in a SOFC with an anode substrate using the sin2ψ method, the cosα method, and Raman spectroscopy. The stress values were generally consistent between the methods, with YSZ having a compressive stress of about 600 MPa. An analysis of the residual stress at high temperatures was attempted using Raman spectroscopy, which, however, was difficult to apply above 700 °C.

Hence, in-situ Raman spectroscopy is an extremely convenient and informative method for assessing mechanical stresses during SOFC operation. The accuracy of this method is at the level of tens of MPa, and both the position and half-width of peaks in Raman spectra can be used as a source of information.

Studies of SOFC anode poisoning with sulfur-containing compounds

One of the urgent problems of SOFC application is poisoning of anodes with sulfur-containing compounds, which are initially included in or subsequently introduced into natural gas or other hydrocarbons used as fuel [44–46]. Raman spectroscopy is often used to study the process of poisoning of solid oxide fuel cells with various compounds. For example, several works examined the poisoning of SOFC anodes with sulfur compounds, and Table 2 contains a brief content of these works. It is evident that the researchers worked over a fairly wide range of both H_2S concentrations, from 0.5 to 100,000 ppm, and operating temperatures, from 300 to 950 °C. Figure 3 shows the operating conditions under which the presented studies were carried out: the H_2S concentration is on a logarithmic scale, and the operating temperature is on a linear scale. It is evident that the vast majority of studies were carried out at temperatures around 700 °C and a hydrogen sulfide content from 30 to 300 ppm.

Hence, the effect of rather low concentrations of H_2S (0.5, 1, and 3 ppm) was studied in [47]. It was shown that between 200 and 400 s after the introduction of sulfur-containing fuel, the open circuit potential (OCP) decreased to about 60% of the initial value, followed by a sharp drop to ~ 10% of the initial OCP between 400 and 450 s. Then, the OCP gradually approached the final value of − 1.07 V over a much longer period of about 1,000 s. The trend of the NiO Raman peak (~ 1100 cm^{-1}) intensity initially increased over the same period of time as the initial slower recovery measured electrochemically. Then, the peak quickly disappeared; however, this sharp drop in the Raman measurement occurred a short time after the sharp drop in the electrochemical potential. This trend was repeated and verified.

In Ref [48]., the degradation behavior was studied as a function of H_2S concentration (5, 10, and 50 ppm) at an operating temperature of 700 °C under constant current load (500 mA/cm^2). When feeding fuel containing H_2S, a rapid voltage drop (the first drop) was observed. With an increase in the H_2S concentration, the voltage drop percentage increased due to a higher sulfur coverage ratio on the Ni surface, and the time required for saturation decreased. A high concentration (50 ppm) of H_2S resulted in an additional voltage loss (the second drop), while the voltage drop was insignificant at low concentrations (5 and 10 ppm). In

Table 2 A summary of the works in which studies of anode poisoning with sulfur-containing compounds were carried out

Concentrations studied, ppm H_2S	Operating temperature, °C	Cell design	Research methods used in addition to Raman spectroscopy	Brief conclusion	Ref.
0.5, 1, 3	715	YSZ-based ESC	IS, SEM, TEM	A correlation was found between the results obtained by electrochemical and optical methods.	[47]
5, 10, 50	700	Ni-YSZ based ASC	Chronopotentiometry, IS, FIB, SEM, EDX	Raman spectra showed that Ni_3S_2 and Ni_3S_4 were formed at both 5 and 50 ppm H_2S due to the reaction of the remaining adsorbed sulfur with nickel during the cooling process. This indicates that the formation of nickel sulfides was not responsible for the second voltage drop.	[48]
50 50	500 570	Ni/YSZ disk	XRD, SEM, EDX	The sulfur poisoning of the Ni–YSZ anode was not due to the formation of conventional nickel sulfides. The sulfide formation and morphological changes observed in the *ex-situ* experiments actually occurred during slow cooling as a result of reactions between bulk Ni and H_2S.	[49]
100 10%	727 950	YSZ-based ESC	XRD, SEM	At a H_2S concentration of 100 ppm, nickel sulfide was formed on the Ni surface, which could block the active oxidation sites of the fuel and impair the performance of the fuel cell. When Ni–YSZ cermet was exposed to hydrogen containing 10% H_2S at 950 °C for 5 days, the Ni particles were completely converted to nickel sulfides.	[50]
100	500	BZCYYb-based ESC	IS, DFT	$-SO_4$ is a key surface functional group on the BZCYYb material that can be removed by a water-mediated process. Direct operand observations and atomistic calculations confirmed the crucial role of water in the sulfur stability of the proton-conducting oxide.	[51]
200	500	3YSZ-based ESC	SEM, chronopotentiometry, IS	The effect of H_2S was very different under open circuit conditions (OCV) and polarization. Compared to the OCV condition, the presence of polarization promoted the formation of nickel sulfide deep inside the anode at the anode/electrolyte interface rather than on the anode surface.	[52]
200	500	YSZ-based ESC	Microphotographs, chronopotentiometry, IS	In the case of polarization, the effect of H_2S on the electrode resistance was much stronger than in the case of OCV.	[53]
300	200 300 500	Ni-CGO disk	Microphotographs, SEM	Raman spectroscopy can be used to monitor the formation of nickel sulfide in-situ at temperatures up to 500 °C. For higher temperatures, optical microscopy can be useful to monitor morphological changes.	[54]

all cases, the performance was not fully restored even after feeding hydrogen fuel without H_2S for ~ 20 h due to incomplete sulfur desorption from the Ni surface. *Post-mortem* analyses were performed on the tested cells. Raman spectra showed that nickel sulfides were formed on both the 5 ppm and 50 ppm tested cells due to the reaction of the remaining adsorbed sulfur with nickel during the cooling process. This indicates that nickel sulfide formation was not responsible for the second voltage drop. SEM/EDX analyses combined with FIB revealed that the second drop was due to oxidation of the outer nickel layer by oxygen ions transported from the electrolyte.

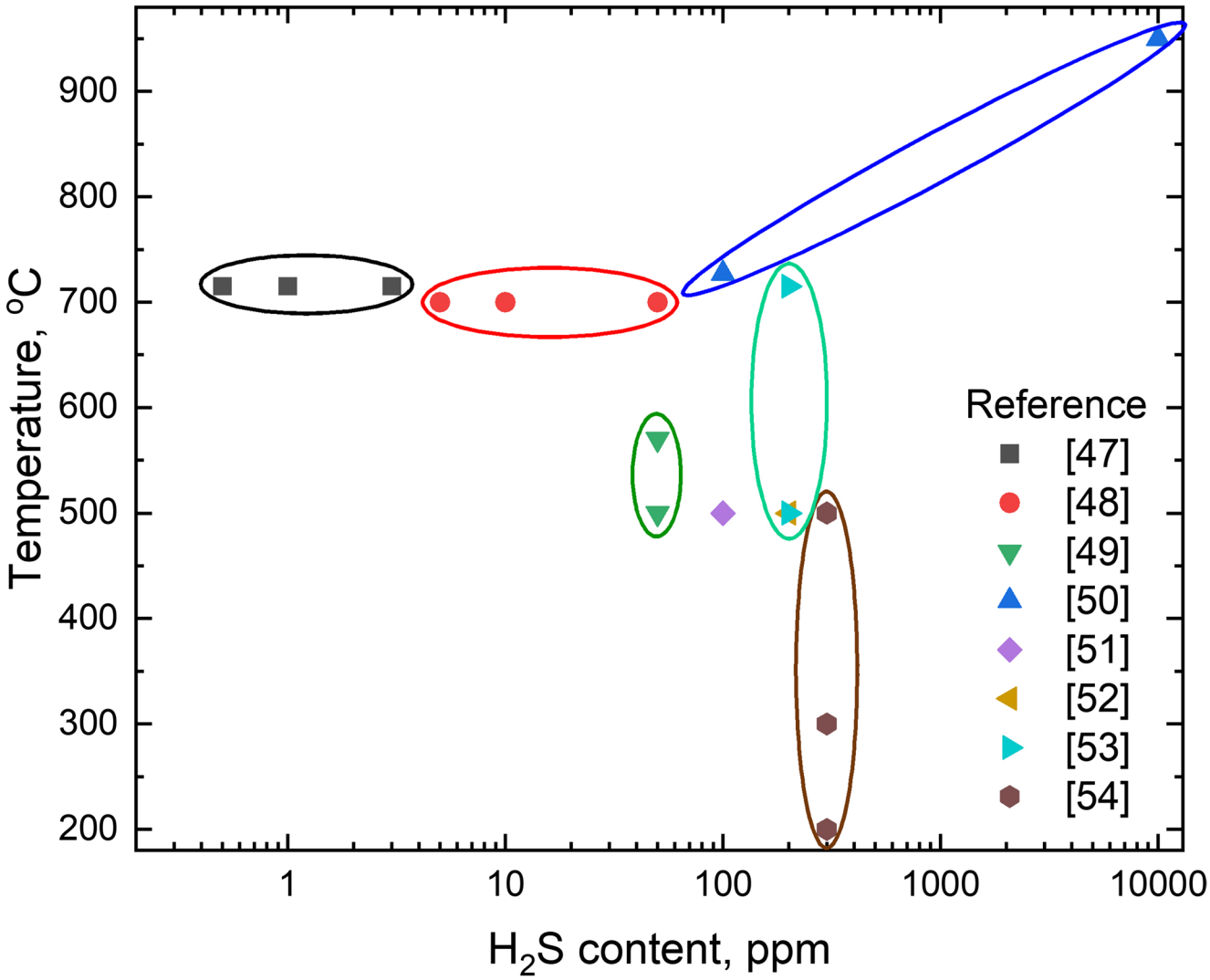

Fig. 3 Operating conditions for studies of SOFC anode poisoning with hydrogen sulfide: content in ppm is on a logarithmic scale and operating temperature is on a linear one

In a more recent paper [49], the authors' group first conducted preliminary studies [50] using *ex-situ* Raman spectroscopy. Of note is the extremely high H_2S content in one of the experiments: 10% (= 100,000 ppm) during exposure at an operating temperature of 950 °C. It was shown that at a H_2S concentration of 100 ppm, nickel sulfide was formed on the Ni surface, which could block active oxidation sites of the fuel (e.g., H_2) and degrade the performance of the fuel cell. When Ni–YSZ cermet was exposed to hydrogen containing 10% H_2S at 950 °C for 5 days, the Ni particles were completely converted to nickel sulfides. Raman spectra show that NiS appeared on the surface of these nickel particles, which is consistent with the prediction of the Ni–S phase diagram. In a later work [49], various bulk nickel sulfides and significant morphological changes were observed on the nickel surfaces of Ni–YSZ composites after exposure to 100 ppm H_2S fuel at elevated temperatures using in-situ Raman microspectroscopy and several *ex-situ* characterization techniques. It was shown that sulfur poisoning of the Ni–YSZ anode was not due to the formation of conventional nickel sulfides. The sulfide formation and morphological changes observed in the *ex-situ* experiments actually occurred during slow cooling as a result of reactions between bulk Ni and H_2S.

A similar concentration of H_2S – 100 ppm – was applied in the study [51] at an operating temperature of 500 °C for a proton conducting system. It was found that the $-SO_4$ group was a key surface functional group on the BZCYYb material that can be removed by a water-assisted process. Direct operand observations and atomistic calculations confirmed the crucial role of water in the sulfur tolerance of the proton-conducting oxide. The strategy of removing elemental sulfur (S*) from the anode surface by oxygen anion flux alone may not be sufficient to achieve complete sulfur tolerance.

Therefore, water-assisted sulfate conversion should be considered as an alternative approach to achieve reliable anode performance in sulfur-containing fuels.

In [52], the Raman studies of SOFC anode poisoning with H2S were carried out in-situ; a combination of Raman spectroscopy studies and electrochemical studies was used. A fairly high concentration of the poisoning compound of 220 ppm was used in the work. Note that a fairly low operating temperature for SOFCs of 500 °C was used. It was shown that the effect of using H_2S differed greatly under open-circuit conditions (OCV) and polarization. For the cell under OCV, a clear correlation was seen between the electrical properties and the amount of nickel sulfide. The saturation of nickel sulfide on the surface corresponded to the shape of the impedance of two intersecting capacitive arcs. The concentration resistance developed almost in the same trend with the amount of nickel sulfide. H_2S reacted with Ni mainly on the electrode surface. In the cell under polarization of 500 mV, a sharp loss of cell current was explained by a significant increase in the charge transfer resistance during the first 7 h. The strong broadening of the impedance spectrum from 16 h in H_2S may correspond to the densification of the entire anode volume of the (Ni, S) phase. Compared to the OCV condition, the presence of polarization favored the formation of nickel sulfide deep inside the anode at the anode/electrolyte interface rather than on the anode surface. This behavior was presumably explained by the presence of NiO on the surface of Ni grains in the cell under polarization of 500 mV. Preliminary studies were performed in [53] using the same H_2S concentration and the same operating temperature. Surprisingly, it was shown that the first step was a decrease in the electrode impedance. This decrease corresponded to the absence of the Raman spectrum of Ni_3S_2. When this Raman spectrum appeared and its intensity increased, the electrode impedance was approximately stable. The impedance increased only when the Raman spectrum of Ni_3S_2 was saturated. All of these effects were localized in the low-frequency part ($< \sim 1$ Hz) of the impedance spectrum attributed to the concentration impedance. With polarization, the effect of H_2S on the electrode resistance was much stronger, multiplying by 10 in about 20 h. However, the measured intensity of the Raman band of Ni_3S_2 was low.

In [54], in-situ studies were performed at a lower operating temperature of 300–500 °C and a higher concentration of the poisoning impurity of 300 ppm H_2S. It was shown that Raman spectroscopy can be used to monitor the formation of nickel sulfide in-situ at temperatures up to 500 °C. At higher temperatures, optical microscopy can help to monitor morphological changes. The morphology study implies that the degree of Ni sulfidation strongly depends on temperature. The strongest sulfidation occurs at 500 °C with a Ni_3S_2 layer covering the sample surface and an enormous grain growth. High temperatures (750–790 °C) facilitate the reaction between H_2S and GDC. The sulfidation process probably involves the diffusion of nickel to sulfide species.

Hence, in-situ Raman spectroscopy allows studying the poisoning of SOFC anodes with sulfur-containing compounds in extremely wide concentration ranges, from at least 0.5 to 10,000 ppm. In combination with more traditional electrochemical techniques, the method enables a detailed study of degradation mechanisms, determination of various compounds formed during poisoning (e.g., nickel and sulfur), and detection of their removal under special conditions.

Studies of SOFC poisoning with chlorine-containing compounds

Investigations of SOFC poisoning using in-situ Raman spectroscopy are not limited to sulfur-containing compounds. A number of works have studied the effect of chlorine-containing compounds. This problem is also extremely relevant for the creation of reliable electrochemical devices with a long service life [55–57]. Table 3 contains a brief summary of these works.

Hence, poisoning with CH_3Cl at a concentration of 110 ppm and an operating temperature of 650 °C was investigated [58]. The poisoning impurity was mixed with both methane and hydrogen fuels. In-situ Raman spectroscopy data showed the loss of observable carbon during the entire CH_3Cl exposure. Poisoning with chlorine was reversible in the early stages of exposure, enabling some recovery after the removal of the chlorine contaminant from the supplied fuel. Catastrophic corrosion of the metal due to carbon deposition supported by the presence of chlorine was proposed as the main degradation method for the SOFC anode. Different mechanisms of degradation of SOFC characteristics were also shown in [59] when operating on hydrogen and on methane containing CH_3Cl.

In a later study [60] by the same authors, the effects of high concentrations of the toxic impurity, from 100 to 300 ppm, at high operating temperatures, from 650 to 700 °C, were examined. It was shown that chlorine significantly affected the performance of SOFCs operating on CH_4. Degradation when operating on CH_4 was significantly faster than when operating on pure H_2 alone. As for the operation on hydrogen, the adsorption of chlorine on the nickel surfaces of the anode led to rapid and reversible degradation, followed by a slower degradation mechanism caused by the sublimation of volatile nickel chloride compounds. Regarding the operation on methane, the inability of chlorine-coated nickel to split CH_4 resulted in fuel starvation during cell polarization. It is this mechanism that is responsible for

Table 3 A summary of the works in which studies of SOFC poisoning with chlorine-containing compounds were carried out

Concentrations studied, ppm CH_3Cl	Operating temperature, °C	Cell design	Research methods used in addition to Raman spectroscopy	Brief summary	Ref.
110	650	ESC	IS, linear sweep voltammetry	In-situ Raman spectroscopy data showed a loss of observable carbon throughout the duration of CH_3Cl exposure. The poisoning was reversible in the early stages of exposure, enabling some recovery once the contaminant was removed from the fuel.	[58]
100, 300	700	ESC	IS, linear sweep voltammetry, NIR, FTIR, FE-SEM	A different mechanism of degradation of SOFC characteristics was shown when operating on hydrogen and on methane containing CH_3Cl.	[59]
100, 300	650–700	ESC	linear sweep voltammetry, thermal imaging, mid-infrared spectroscopy	CH_3Cl resulted in reduced anode cooling in thermal imaging, suppressed carbon accumulation in Raman spectroscopy, and lower fuel consumption and oxidation product formation based on mid-IR spectroscopy results.	[60]

the accelerated degradation rate observed when operating on CH_4 compared to H_2.

The experimental results [58–60] were summarized by the authors in Ref [60]. It was demonstrated that the effects of chlorine included reduced anode cooling in thermal imaging, suppressed carbon accumulation in Raman spectroscopy, and lower fuel consumption and oxidation product formation based on mid-IR spectroscopy results. For chlorine poisoning, degradation was more irreversible at 700 °C than at 650 °C, a result that is attributed to sublimation and irreparable loss of anode material at the higher temperature.

These results lead to an intermediate conclusion that in-situ Raman spectroscopy enables one to study successfully the poisoning of SOFC anodes with chlorine-containing fuel impurity compounds. It is also worth noting the possibility of studying combined poisoning with chlorine and carbon deposition on the SOFC anode when the poisoning factors can act together with various mutual influences.

Carbonization of SOFC anodes in hydrocarbon-containing fuels

The study of the deposition of carbon in SOFC anodes, which is part of hydrocarbon fuel, is an extremely urgent and important task in creating durable and reliable SOFCs [61–63]. Raman spectroscopy enables a sufficiently detailed analysis of the mechanisms of processes occurring at the micro-level and provides unique in-situ information that is not available for the vast majority of other methods. Table 4 contains a brief description of the works in which in-situ Raman spectroscopy was used to study the process of carbon deposition on SOFC anodes using various types of hydrocarbons as fuel.

The undisputed classical works on carbon deposition at SOFC anodes using in-situ Raman spectroscopy were made by the group headed by Professor R.A. Walker from Montana University. In their pioneering work [64] published in 2006, it was shown that the cermet anode of SOFC exposed to C_4H_{10} exhibited the presence of carbon on the surface, as indicated by the characteristic D and G bands of carbon [92, 93]. The integrated intensities of the D and G bands indicated the amount of "disordered" (or sp^3) carbon relative to the amount of ordered (or sp^2 "graphite") carbon, respectively. A D/G ratio of 1.3 corresponded to an average domain size of 3–4 nm.

In an inert or reducing atmosphere (Ar or H_2 in Ar), the signatures of deposited carbon remained stable for several hours. However, the introduction of an oxidizer into the gas atmosphere above the carbon-containing Ni/YSZ cermet resulted in rapid degradation of the carbon deposits and the growth of NiO. Shortly after introducing water into the Ar gas flow, the intensity of the carbon bands decreased, and a NiO band began to appear at around 1060 cm^{-1} [94, 95]. Given the absence of carbon signatures in the second spectrum after the introduction of water, the authors conclude that the carbon deposits disappeared from the Ni/YSZ surface.

In the work [65] by the same group, C_4H_{10} was also used as a model fuel. Both C_4H_{10} and CO were shown to form graphitic intermediates, but under very specific and very different conditions. In the high CO flux limit, excess butane formed ordered graphite, but only temporarily. At higher cell potentials (i.e., lower overpotentials), both ordered and disordered graphite were formed at the nickel anode after exposure to butane. Those deposits were oxidized if the cell continued to operate without a carbon source while fuel was being supplied. Most of the graphite was formed at the nickel

Table 4 A summary of the studies on carbon deposition at the SOFC anodes

Operating temperature, °C	Fuel	Peculiarity of the work	Brief conclusion	Ref.
715	C_4H_{10}	pioneering work in this direction	The presence of carbon on the surface of the cermet anode after C_4H_{10} was shown, as indicated by the characteristic D and G bands. The integrated intensities of the D and G bands indicated the amount of "disordered" (or sp^3) carbon relative to the amount of ordered (or sp^2 "graphitic") carbon, respectively. A D/G ratio of 1.3 corresponded to an average domain size of 3–4 nm. In an inert or reducing atmosphere, the signatures of deposited carbon remained stable for several hours. However, the introduction of an oxidizer into the gas atmosphere above the carbon-containing cermet resulted in rapid degradation of the carbon deposits and the growth of NiO.	[64]
715	C_4H_{10} Ar/H_2	first direct in-situ measurements of chemical intermediates at SOFC anodes under real operating conditions	Fuels of C_4H_{10} and CO formed graphitic intermediates, but under very specific and very different conditions. In the high CO flux limit, excess butane formed ordered graphite, but only temporarily. At lower anode overpotentials, both ordered and disordered graphite were formed after exposure to butane. Most of the graphite was formed on Ni anodes under OCV conditions, the distribution being heavily biased towards disordered graphite.	[65]
715	CH_4/C_2H_4, CH_4/C_3H_6, C_2H_4/C_3H_6	complex fuel mixtures	The electrochemical behavior of SOFCs operating on C_4H_{10} was duplicated by a stoichiometric fuel mixture of C_2H_4 and C_3H_6. Methane CH_4 had little effect when mixed with other components of the flow after C_4H_{10} pyrolysis. In terms of the amount of disordered phase, the graphite structures formed after C_4H_{10} feeding can be duplicated by both C_3H_6 alone and CH_4/C_3H_6 and C_2H_4/C_3H_6 mixtures. However, the current recovery and power density observed with C_4H_{10} are duplicated only when the fuel mixture contains C_2H_4 and C_3H_6. The recovery is thought to result from a conducting graphite network across the anode with sufficient disorder to act as a current collector.	[66]
715	CH_4 C_2H_4 C_3H_6		Most of the pyrolysis products of C_4H_{10}/CH_4, C_2H_4, and C_3H_6 formed different carbon deposits that had different effects on the performance of the Ni/YSZ anode. Methane CH_4 formed small amounts of highly ordered graphite that had little effect on cell performance compared to other fuels. Ethylene C_2H_4 produced larger carbon deposits with slightly more disorder, and those deposits had a detrimental effect on electrochemical performance. The structure of the carbon deposits formed by C_2H_4 changed with exposure. Propylene C_3H_6 formed disordered carbon deposits that were structurally similar to those produced by C_4H_{10}. The performance of cells operating on C_3H_6 continued to decline with continued exposure to hydrocarbon fuels and did not recover. This behavior contrasts with the performance of cells exposed to comparable amounts of C_4H_{10}. The initial stages of carbon formation depend on the chemical nature of the fuel, and both the type of carbon formed and its amount are important when considering the effect of graphite formation on the electrochemical performance.	[67]
715	CH_4 CH_3OH	NIR + RS	Devices designed to operate with CH_3OH must employ steps to ensure that the fuel undergoes sufficient pretreatment to inhibit carbon growth. These steps may include steam and carbon dioxide reforming, as well as operation at higher temperatures. The carbon deposits were identified as graphitic, with those from CH_4 being highly ordered and those from CH_3OH having a slight degree of disorder. In the early stages, carbon formed from CH_4 and CH_3OH grew at the same rate. Pure formation of graphite from CH_4 was self-limiting, given that the spectral intensity ceased to increase after about 5 min. However, graphite formed from CH_3OH appeared to be formed via multiple pathways, given the rapid onset of additional intensity in the spectra obtained after about 5–7 min. This result was interpreted in terms of the relatively greater reactivity of the CH_3OH-based fuel mixture, as well as the weaker bond enthalpies in CH_3OH.	[68]

Table 4 (continued)

Operating temperature, °C	Fuel	Peculiarity of the work	Brief conclusion	Ref.
715	C_2H_5OH	use of ethanol as fuel	Before reaching the anode, C_2H_5OH formed a mixture of CO, CH_4, CO_2, and C_2H_2. When the cell was held at the OCV, wetted C_2H_5OH resulted in rapid growth of graphitic carbon, but device polarization slowed down the carbon growth. The growth was completely suppressed at the highest overpotentials. IS measurements showed that rapid carbon growth was accompanied by a significant reduction in performance. However, this effect was much less noticeable in polarized cells, even when the Raman data showed the clear presence of carbon deposits. A dry ethanol feed contained significantly more C_2H_2 as a pyrolysis product. That feed resulted in immediate formation and rapid growth of graphite regardless of cell polarization.	[69]
725	CH_4	"spectrochronopotentiometry"	RS identified the carbon formed from dry CH_4 as highly ordered graphite. An increase in the exposure time led to a proportional decrease in the electrochemically available carbon. The accumulated graphite could be used as fuel, allowing the SOFC to operate stably and reversibly. Excessive carbon formation and subsequent electrochemical oxidation resulted in significant and irreversible damage to the SOFC even after the carbon had been oxidized.	[70]
730	CH_4		Optically and electrochemically, significant and reproducible differences in the carbon removal rates of H_2O, CO_2, and O_2 were shown. All three reformers removed carbon; however, O_2 was also quite aggressive toward the anode and significantly oxidized the anode Ni surfaces within minutes. Water H_2O and carbon dioxide CO_2 removed carbon deposits but only partially oxidized Ni, showing a more gentle behavior toward the anode. Carbon removal rates were fastest with H_2O, then O_2, and finally CO_2. These results are consistent with the formation of adsorbed oxygen intermediates as the rate-limiting step in carbon gasification.	[71]
727	H_2 CH_4		Both electrochemical and non-electrochemical oxidation of the fuel and even the Ni anode were possible. The predominance depended on the fuel concentration, cell impedance, and operating potential. A slow linear decline in the graphite signal corresponded to non-electrochemical oxidation of graphite, while rapid sigmoidal drops in the graphite signal occurred through electrochemical oxidation at much lower potentials.	[72]
675	CO/H_2	high load currents	Carbon was readily formed on anodes maintained at OCV, and the carbon deposits consisted of highly ordered graphite. The polarization of the SOFC limited the amount of carbon formed: at currents approaching 75% of I_{max}, the observed carbon formation was completely suppressed. Voltammetry data were unstable until a small amount of carbon had been formed.	[73]
800	CH_4, biogas		Nickel is a much more active catalyst for biogas than for CH_4. The detectable carbon formed at polarized and non-polarized SOFC anodes showed significantly less CO_x emitted by anodes exposed to biogas compared to CH_4.	[74]
700 800	CH_4, biogas		Carbon growth increased with temperature in methane; however, dry reforming of biogas resulted in lower carbon growth and higher CO mole fractions, especially at high temperatures. The intermediate $Ni-CH_x$ phases were measurable and important in methane degradation but were affected by the operating temperature and CO_2 addition. For biogas, carbon growth was minimal only at lower operating temperatures; for methane, however, carbon formation occurred at all temperatures. Subsequent electrochemical oxidation of the deposited carbon showed that carbon formation was differentially affected by temperature under both fuel conditions. Under methane conditions, carbon accumulation was rapid and not modulated by polarization.	[75]
650	CH_4-CH_3Cl H_2-CH_3Cl	110 ppm CH_3Cl admixture	The loss of observable carbon was shown throughout the CH_3Cl exposure. Both separate degradation mechanisms of chlorine and carbon poisoning acted separately. Moreover, carbon and chlorine appeared to cause extensive and accelerated combined damage to the fuel cell anode.	[58]

Table 4 (continued)

Operating temperature, °C	Fuel	Peculiarity of the work	Brief conclusion	Ref.
800	C_4H_9OH	use of butanol as fuel	Fuel humidification resulted in dramatic changes in the electrochemical performance of the cell, as well as in the Raman spectra. Both fuels (dry and humidified) led to anode cooling of approximately 4 ˚C after 10 min of exposure. However, the Raman data clearly showed that dry butanol exhibited greater carbon accumulation. Humidified butanol did not show any differences, suggesting that heterogeneous surface phase chemistry is responsible for preventing carbon accumulation. Cell polarization was very effective in suppressing the early stages of carbon accumulation when operating with dry butanol.	[76]
730	CH_4	Sn and BaO infiltration	Undoped and 1% Sn anodes were very susceptible to carbon formation from CH_4, while significantly less carbon was accumulated on the 1% BaO anodes. Electrochemical data showed carbon accumulation in different regions of the anode, with Sn and BaO effectively reducing accumulation but also inhibiting electrochemical oxidation. For each anode, H_2O was the most effective reforming agent for carbon removal, followed by O_2 and then CO_2. However, H_2O and CO_2 left the anode only partially oxidized, while prolonged exposure to O_2 completely oxidized Ni to NiO.	[77]
850	CO/CO_2 CH_4	STN electrode	Despite the low nickel concentration, infiltrated nickel oxide particles enhanced coking during exposure to pure methane. The deposited carbon could be partially removed by humidifying steam. The addition of Co addition resulted in the presence of Co_3O_4 in the spectra of the reduced preliminary electrodes. Cobalt oxide Co_3O_4 disappeared during electrode reduction, presumably due to the formation of metallic Co, the electrodes containing Co without any signs of coking.	[78]
750	H_2 CH_4 CO_2/CH_4	STN electrode	Carbon was accumulated on all Ni-containing electrodes when exposed to 100% CH_4. Carbon had a negative effect on STN electrodes impregnated with Ni alone, and a positive effect was observed when Ni was co-impregnated with CGO. Cobalt may be a promising electrococatalyst that prevents coking while maintaining stable performance.	[79]
800	CO/H_2		The CO fuel was used by direct oxidation, which was independent of the amount of CO. During polarization under H_2-rich syngas conditions, the anode surface temperature did not increase as much as it did when operating with H_2 or CO alone. Raman spectra together with "spectrochronopotentiometry" experiments showed that carbon was not observed on the anode surface at 800 °C, although it was observed at 750 °C and 700 °C. However, carbon was likely present in a spectroscopically inaccessible, electrochemically active region at the electrolyte/electrode interface.	[80]
625	CH_4 C_3H_8	mapping BaO modification	Direct evidence of preferential coking on the Ni surface with little or no coking of YSZ: carbon growth on the Ni surface was successfully monitored over time at high temperatures. The hypothesis is that BaO particles help to utilize water to prevent carbon deposition.	[81]
450	C_3H_8	SERS	A study of a polished nickel surface exposed to wet propane at 450 °C was carried out. The D- and G-band increased with time; however, the SERS-activated sample exhibited a much higher intensity and signal-to-noise ratio. A more resolved trend was observed for SERS: carbon was rapidly deposited on the nickel surface initially, and then the deposition rate slowed down with time. Spectra for carbon removal, as well as the integration of the carbon D-band obtained: the carbon peaks decreased with the introduction of oxygen, and most of the deposited carbon was removed within 1,000 s.	[82]
450	C_3H_8	SERS	The onset of coking occurred at the first exposure to propane, and continuous exposure gradually built up carbon deposits. The onset of coking can be suppressed by surface deposition of a thin GDC coating. However, after reoxidation of the modified Ni surface during air exposure followed by reduction for regeneration, the coking resistance was compromised due to the formation of new Ni surfaces. Mapping revealed that the Ni/YSZ interface was more active in carbon deposition and removal than the Ni surface away from the interface.	[83]

Table 4 (continued)

Operating temperature, °C	Fuel	Peculiarity of the work	Brief conclusion	Ref.
450, 600	C_3H_8, H_2, CO_2	proton conductivity	The -OH groups on the BaO surface readily reacted with hydrocarbon molecules or carbon atoms on the Ni surface, providing resistance to coking. The resulting CO_2 reacted with BaO to form $BaCO_3$, which is difficult to regenerate. BZY and BZCYYb retained a significant number of -OH groups when exposed to propane without decomposing into bulk carbonate phases. In addition to the steam reforming mechanism, BZCYYb facilitated the CO_2 reforming of deposited carbon.	[84]
500	C_3H_8	addition of the proton conductor $SrZr_{0.95}Y_{0.05}O_{3-x}$ (SZY) to the anode	The -CO_3 groups on the surface of SZY oxidized the deposited carbon. After depletion, -CO_3 could be regenerated through a reaction between H_2O at low concentrations and deposited carbon around an electrochemically inactive region where there was an insufficient supply of oxide ions. In the inactive region, H_2O oxidized carbon to oxide.	[85]
600	CO		The anode was exposed to CO. Instead of continuing to increase in intensity, the carbon peaks quickly stabilized: carbon formation did not continue indefinitely under these conditions. As expected, a large initial increase in the OCV was observed when the fuel was replaced by CO due to the difference in oxidation kinetics between CO and H_2. The D peak was much smaller than the G peak (D/G of about 0.2). This, combined with the intense and sharp peaks, indicates that carbon was formed in the graphitic form.	[24]
600	CO H_2-CO H_2		There were clear differences in the dynamics of carbon deposition depending on the operating parameters, such as current load and fuel composition. The RS was used to study the removal of surface carbon from SOFC anodes using electrochemical oxidation.	[86]
600	CO		Carbon formation was initially rapid and then stabilized. Under these conditions, the process was largely self-limiting. Polarization of the anodes resulted in a significant reduction in carbon formation. Mapping of the surfaces of polarized anodes with distinct regions without carbon and heavy carbon deposits was carried out. Carbon was predominantly formed in the regions where gas access was limited.	[23]
500	CO_2/CO	SOEC	The charge transfer reactions for TPB in the CO_2 electrolysis mode promoted carbon deposition because of local changes in the gas composition. Most of the carbon was formed near the electrode/electrolyte interface. The CGO intermediate layer reduced carbon deposition in Ni/CGO electrodes and improved mechanical stability under CO–CO_2 electrolysis conditions.	[87]
750	CO_2/CO	SOFC/SOEC	For the SOEC mode, carbon deposition could be be greatly enhanced by overpotential, and the carbon deposited was heavier near the TPB than in the middle of the Ni strips. In contrast, for the SOFC mode, the deposited carbon could be directly consumed by electricity, and the carbon content near the TPB was lower than that in the middle of the strips.	[88]
	CO_2/CO	SOEC	*Ex-situ* measurements for CO_2/CO electrolysis revealed the presence of both disordered and graphitic carbon on the nickel electrode surface.	[89]
	CH_4	Mesh-shape electrode	During the OCV condition, carbon began to deposit on the surface of the nickel mesh electrode. The deposition was clearly recorded by the emergence of a specific peak at ~ 1560 cm^{-1}. The carbon was in the form of graphite, and the coating on the surface was non-uniform: it changed from grain to grain. When anodic overpotential was applied to the electrode, the carbon gradually disappeared from the edge of the electrode, i.e., from the electrode/electrolyte interface, where oxygen was electrochemically supplied. This is the first in-situ observation of the electrochemical oxidation of carbon under real operating conditions.	[90]
750	CH_4-H_2	optically transparent solid electrolyte, information from the internal interface	The addition of methane led to the formation of CO and an increase in the H_2 content in the reaction products. A more significant decrease in the CH_4 content relative to the increase in the H_2 and CO concentrations may be due to the Boudoir reaction and carbon deposition since the electrochemical performance of the SOFC deteriorated over time due to anode carbonization.	[91]

anodes under OCV conditions, and the distribution was heavily biased towards disordered graphite. The chemistry of CO oxidation should be simpler, given that CO requires the addition of one oxygen to form CO_2. At intermediate cell potentials, ordered graphite was formed, and the target intermediate on the path to CO oxidation appeared. These compounds did not appear at higher or lower cell potentials. Taken together, the results presented in this work are the first direct in-situ identification of the chemical species present in SOFCs operating under real conditions.

A slightly later study [66] examined more complex fuel mixtures. It was shown that the electrochemical behavior resulting from SOFC operation on butane was duplicated by a stoichiometric fuel mixture of ethylene and propylene. Methane had little effect when mixed with other components of the butane pyrolysis stream and made a minimal contribution to the chemical mechanisms of fuel breakdown and oxidation in SOFCs operating on high-weight hydrocarbons. In terms of the amount of disordered phase, the graphitic structures formed from the butane feed can be duplicated by propylene alone, as well as by mixtures of methane/propylene and ethylene/propylene. However, the current recovery and power density observed with butane are duplicated only when the fuel mixture contains ethylene and propylene. The recovery is thought to result from a conducting graphite network across the anode with sufficient disorder to act as a current collector.

In a summary of these studies [67], it was shown that most of the pyrolysis products of butane – methane, ethylene, and propylene – formed a variety of carbon deposits that had different effects on the performance of the Ni/YSZ SOFC anode. Methane formed small amounts of highly ordered graphite, which had little effect on cell performance compared to other fuels. Ethylene produced larger carbon deposits with slightly more disorder, and those deposits had a detrimental effect on electrochemical performance. The structure of the carbon deposits formed by ethylene changed with exposure. Propylene, on the other hand, formed disordered carbon deposits that were structurally similar to those produced by butane. The performance of cells fed with propylene continued to decline with continued exposure to hydrocarbon fuels and did not recover. This behavior contrasts with the performance of cells exposed to comparable amounts of butane. Taken together, this suggests that the initial stages of carbon formation at Ni/YSZ anodes depend on the chemical nature of the supplied fuel and that both the 'type' of carbon formed (ordered or disordered) and the amount of carbon deposited are important when considering the influence of graphite formation on the electrochemical performance of SOFCs.

Methane and methanol were studied as fuels in [68]. It was shown that devices designed to operate with methanol must employ steps to ensure that the fuel undergoes sufficient pretreatment to inhibit carbon growth. These steps may include steam or carbon dioxide reforming, as well as operation at higher temperatures.

In-situ Raman data identified the carbon deposits as graphitic, with methane-derived deposits being highly ordered and methanol-derived deposits having a low degree of disorder. Early on, methane- and methanol-derived carbon grew at similar rates. Net formation of graphite from methane was self-limiting, given that the spectral intensity ceased to increase after about 5 min. However, methanol-derived graphite appeared to be formed via multiple pathways, given the rapid onset of additional intensity in the spectra obtained after about 5–7 min. This result was interpreted in terms of the relatively greater reactivity of the methanol-derived fuel mixture, as well as the weaker binding enthalpies in methanol.

In a study by the same group of authors [69], the behavior of SOFCs operating on ethanol was examined. Both dry and humidified ethanol were shown to form a mixture of CO, CH_4, CO_2, and C_2H_2 before reaching the anode. When the cell was held at the OCV, humidified ethanol resulted in rapid growth of graphitic carbon, but polarization of the device slowed down the carbon growth. The growth was completely suppressed at the highest overpotentials. Impedance spectroscopy measurements showed that the rapid growth of carbon deposits was accompanied by a significant decrease in performance. However, this effect was much less noticeable in polarized cells, even when the Raman data showed the clear presence of deposits. The dry ethanol feed contained significantly more acetylene as a pyrolysis product. This feed resulted in immediate formation and rapid growth of graphite, regardless of cell polarization.

A group of authors led by R.A. Walker continued the study of methane, which was used as a fuel, in [70]. For the first time, they used a combined technique called "spectrochronopotentiometry" was used, which is the correlation between electrochemical characteristics and spectral properties measured in-situ. Raman spectroscopy identified the carbon formed from dry methane as highly ordered graphite. It was shown that an increase in the the exposure time led to a proportional decrease in the electrochemically available carbon and that the accumulated graphite could be used as a fuel, allowing the SOFC to operate stably and reversibly. However, excessive carbon formation and subsequent electrochemical oxidation resulted in significant and irreversible damage to the SOFC even after the carbon had been oxidized.

The paper [71] is devoted, in turn, to the removal of formed carbon. Significant and reproducible differences in the rates of carbon removal by agents such as H_2O, CO_2, and O_2 were observed in both the spectroscopic graphite

signatures and the simultaneous changes in the cell OCV; both optical and electrochemical methods were used. All three reforming agents tested in that work removed carbon from SOFC anodes. However, oxygen also behaved quite aggressively towards the anode and noticeably oxidized the anode nickel surfaces within a few minutes. In contrast, water and carbon dioxide removed carbon deposits but only partially oxidized nickel, showing that carbon removal by these two reforming agents was more gentle on the anode than oxygen. Carbon removal rates were fastest with H_2O, then O_2 and finally CO_2. These results, combined with earlier work on oxygen dissociation over catalytic Ni [96, 97], are consistent with the formation of adsorbed oxygen intermediates as the rate-limiting step in carbon gasification. The consistently observed delay in carbon removal by oxygen may indicate that the oxides stabilized by the step edges must reach a threshold population before they can "spill over" to react with the adsorbed carbon. Once this spillover effect occurs, carbon oxidation occurs rapidly. Subsequent Ni oxidation also occurs more rapidly and is most intense under O_2.

The mechanisms of SOFC fuel and nickel anode oxidation were studied in [72]. The authors demonstrated that both electrochemical and non-electrochemical oxidation of the fuel and even the SOFC nickel anode could occur and that the dominance of any given mechanism was a function of the fuel concentration, cell impedance, and operating potential. Slow linear depletion of the graphite signal corresponded to non-electrochemical oxidation of graphite via oxide recombination to molecular oxygen, followed by the reaction of molecular oxygen with carbon to form CO_2, while the rapid sigmoidal drops in the graphite signal occurred via electrochemical oxidation at much lower potentials.

The authors of the paper [73] used model CO/H_2 synthesis gas mixtures and fairly high load currents. It was shown that carbon was formed quite easily on anodes held at OCV and that the carbon deposits consisted of highly ordered graphite. The polarization of the SOFC limited the amount of carbon formed. At currents approaching 75% of I_{max}, where I_{max} corresponds to zero potential difference between the cathode and anode, the observed carbon formation was completely suppressed. Interestingly, the voltammetry data from the studied assemblies with anode support were unstable until a small amount of carbon was formed.

In the work [74] by the same group of authors, the performance of SOFCs on methane and model biogas was compared. It was shown that nickel was a much more active catalyst for biogas than for methane. The detectable carbon formed at polarized and unpolarized SOFC anodes and the Fourier transform infrared spectroscopy (FTIR) spectra from polarized cells showed significantly less CO_x emitted by the anodes exposed to biogas compared to methane. Since carbon growth is well known to be detrimental to SOFC performance, these results point to the advantages associated with natural reforming in SOFC systems operating on biogas.

These comparative studies using methane and biogas were continued in [75]. It was demonstrated that carbon growth increased with temperature when using methane; however, dry reforming of biogas resulted in lower carbon growth and higher overall CO mole fractions, especially at high operating temperatures. Based on the temperature dependence of the dry reforming reaction products and the associated carbon growth, it was concluded that the process was modulated by the Boudoir reaction, although the water-gas shift reaction (WGSR) might contribute as well. Raman spectroscopy showed that the intermediate $Ni-CH_x$ phases were measurable and important in methane degradation but were affected by operating temperature and CO_2 addition. For the biogas case, carbon growth was minimal only at lower operating temperatures. However, under methane conditions, carbon formation occurred at all temperatures. Subsequent electrochemical oxidation of the deposited carbon showed that carbon formation under the conditions of both types of fuel depended differently on temperature: for methane, carbon accumulation occurred rapidly and was not modulated by polarization.

The combined use of chlorine poisoning compounds and carbon deposition on the anode of a SOFC was investigated in [58]. In-situ Raman spectroscopy data revealed a loss of observable carbon throughout the CH_3Cl exposure. The primary objective of this study was to determine whether there were coupled effects between the chlorine and carbon poisoning mechanisms. It was shown that both separate degradation mechanisms were present and that carbon and chlorine appeared to co-induce extensive and accelerated damage to the fuel cell anode, i.e., catastrophic metal corrosion by carbon deposition supported by chlorine loading.

The same group of authors in [76] used a rather specific composition of fuel – C_4H_9OH. There are very few known works with such a specific fuel [98–100]; some of them are simulations, but not experimental ones. It was shown in that work that fuel humidification led to drastic changes in the electrochemical characteristics of the cell, as well as in the Raman spectra. Both types of fuel (dry and humidified) resulted in cooling of the anode by about 4 °C after 10 min of exposure, and the Raman data clearly showed that dry butanol exhibited greater carbon accumulation. No clear features were observed in the Raman spectra obtained from cells operating with humidified butanol, suggesting that heterogeneous surface phase chemistry and, in particular, vapor dissociation at the anode surface, as well as Boudoir reactions, are responsible for preventing carbon accumulation

under these conditions. Cell polarization was very effective in suppressing the early stages of carbon accumulation on the anodes operating with dry butanol.

In [77], a fairly conventional fuel, methane, was used, but an interesting feature was the impregnation of the anodes with tin and barium oxide. It was demonstrated that undoped and 1% tin-impregnated anodes were very susceptible to carbon formation from methane, while significantly less carbon was accumulated on the 1% barium oxide-impregnated anodes. The electrochemical data, however, showed that carbon was accumulated in different regions of the anode and that both Sn and BaO were effective in reducing carbon accumulation but also inhibited electrochemical oxidation. For each anode, water vapor was the most effective reforming agent for carbon removal, followed by oxygen and then carbon dioxide. However, H_2O and CO_2 left the anode only partially oxidized, while prolonged exposure to O_2 completely oxidized nickel to the oxide.

The paper [78] is attractive due to the choice of a rather rare fuel electrode composition – niobium-doped strontium titanate (STN). This composition has rarely been studied in the literature [101–103] compared to the traditional nickel-cermet anode. The paper demonstrated that nickel oxide particles infiltrated into STN promoted coking during exposure to pure methane as a fuel, although the nickel loadings were so low that the expected vibrational characteristic of NiO could not be observed in pre-reduced anodes. The deposited carbon could be partially, but not completely, removed by water vapor. Similar cobalt loadings in STN showed the presence of Co_3O_4 in the Raman spectra recorded on pre-reduced electrodes. Cobalt oxide Co_3O_4 disappeared upon electrode reduction, presumably due to the formation of metallic cobalt. Moreover, electrodes containing this metal showed no signs of coking within the resolution of Raman spectroscopy when exposed to methane.

The investigations initiated in [78] were continued in the subsequent paper [79]. The Raman spectra clearly showed that carbon was accumulated on all Ni-containing electrodes when exposed to pure methane. While carbon had a negative effect on STN impregnated with Ni alone, a positive effect was observed when Ni was co-impregnated with GDC. This result was attributed to an expected increase in the electrochemically active region due to better electrical connectivity in the presence of carbon and/or increased oxygen exchange activity due to the resulting low oxygen partial pressure. The results also indicate that cobalt may be a promising electrococatalyst that prevents coking while maintaining stable performance, making this element an interesting candidate for the development of carbon-tolerant SOFC anodes.

In [80], model CO/H_2 synthesis gas with different hydrogen contents, as well as pure hydrogen and carbon monoxide, was used as fuel. The results obtained using pure CO showed that CO was utilized by direct oxidation, which was independent of its amount. During polarization under conditions of using hydrogen-rich synthesis gas as a fuel, the anode surface temperature did not increase as much as it did when working with only pure hydrogen or carbon monoxide. This result can be explained by the formation of water from the electrochemical oxidation of H_2, which participates in the endothermic gasification of adsorbed carbon. These reactions probably occurred in the electrochemically active region of the anode. SOFCs operating on synthesis gas were compared with those using H_2 and CO separately. Raman spectra together with "spectrochronopotentiometry" experiments [70] showed that carbon was not observed on the anode surface at an operating temperature of 800 °C, although it was observed at 750 °C and 700 °C. However, carbon was probably present in a spectroscopically inaccessible, electrochemically active region at the "electrolyte/electrode" interface. The region was inaccessible due to the low penetration depth of the excitation and scattered radiation [104–106].

A fairly wide range of studies on anode carbonization using various hydrocarbons as fuels has been carried out by a group led by Professor Meilin Liu. The preparatory works include [107] and [108]. In these works, a technique for using SERS (surface-enhanced Raman scattering) [109–111] was developed, and preliminary *ex-situ* studies were carried out. For example, $Ag@SiO_2$ was used as SERS particles [112–114]. Using the results of the preparatory works, the paper [81] provided direct evidence of preferential coking on the Ni surface with little or no coking of YSZ, and carbon growth on the Ni surface was successfully monitored over time at high temperatures. Raman spectroscopy also provided additional evidence of the roles that water and BaO modification played in the coking resistance of the Ni anode. The hypothesis is that the BaO particles help to utilize water to prevent carbon deposition. This result provides useful information for further improvement of the anode design.

In [82], as in the previous work [81], propane was used as a model fuel. Classical Raman and time-resolved SERS were used for studies on a polished nickel surface exposed to wet propane at an operating temperature of the SOFC of 450 °C. In both cases, the D- and G-bands of carbon increased with time; however, the SERS-activated sample exhibited a much higher intensity and signal-to-noise ratio. The signal strength of both the D-band of carbon and the G-band increased significantly with time. The signal intensity from the SERS-activated sample showed a more resolved trend: carbon was rapidly deposited on the nickel surface initially, and then the deposition rate slowed down with time. Time-resolved Raman and SERS spectra of the

carbon removal experiment, as well as the integration of the D-band of carbon, were presented. In both cases, the carbon peaks decreased with the introduction of oxygen. As can be seen from the SERS data, most of the deposited carbon was removed within 1,000 s.

In [83], the coking studies under propane operation were continued. It was shown that the onset of coking occurred upon first exposure to propane and that continuous exposure led to gradual addition of the carbon deposit. Coking onset can be suppressed by surface deposition of a thin GDC coating. However, after the GDC-modified nickel surface was reoxidized during air exposure followed by reduction for regeneration, coking resistance was compromised due to the formation of new nickel surfaces. Carbon signal mapping on a structured Ni–YSZ anode revealed that the Ni/YSZ interface was more active in carbon deposition and removal than the nickel surface away from the Ni/YSZ interface. In particular, the Ni/YSZ interface appeared to catalyze hydrocarbon reforming, resulting in the accumulation of a few hydrocarbon molecules that can be completely removed by applying an anodic current.

An interesting feature of the work [84] is the study of SOFCs with a proton-conducting electrolyte. It was demonstrated that while numerous –OH groups on the BaO surface readily reacted with hydrocarbon molecules in the gas or carbon atoms on the nickel surface providing resistance to coking, the resulting carbon dioxide reacted with BaO to form barium carbonate, which is difficult to regenerate. In contrast, BZY and BZCYYb powders retained a significant number of –OH groups when exposed to propane without decomposing into bulk carbonate phases. In addition to the steam reforming mechanism, BZCYYb facilitated the carbon dioxide (dry) reforming of deposited carbon.

The paper [85] by the same group of authors is notable for the addition of the catalytically active material, $SrZr_{0.95}Y_{0.05}O_{3-x}$ (SZY), to the anode [115–117]. The paper demonstrated that -CO_3 groups on the surface of SZY oxidized deposited carbon to carbon monoxide. Once depleted, these -CO_3 groups could then be regenerated by a reaction between low-concentration water vapor and deposited carbon around an electrochemically inactive region where there was an insufficient supply of oxide ions. In the inactive region, water vapor also oxidizes deposited carbon to carbon monoxide. The reversibility and repeatability of these reactions explain the long-term coking resistance observed with SZY infiltration into the Ni-YSZ anode.

Another group that has systematically investigated anode carbonization using different hydrocarbon fuels is the team led by Professors N.P. Brandon and L.F. Cohen from Imperial College. In [24], the SOFC anode was exposed to CO, and a strong initial growth of carbon was observed on the anode surface, as indicated by the sharp emergence of both D and G peaks. However, rather than continuing to grow, these peaks quickly stabilized, suggesting that carbon formation did not continue indefinitely under these conditions. A large initial increase in the OCV was observed when the fuel was changed to CO due to the differences in oxidation kinetics between CO and H_2. Over longer time scales, a small increase in the cell OCV is observed, indicating a slow, long-term degradation of electrochemical performance. However, that was not noticeable in the Raman signal, suggesting that it might be due to pore closure occurring within the anode below the detection depth available for Raman spectroscopy. The D peak was much smaller than the G peak (D/G ratio of about 0.2). This, combined with the intense and sharp peaks, indicates that carbon was formed predominantly in the graphitic form.

In the work [86] by the same group of authors, the operation of SOFCs on pure carbon monoxide, its mixture with hydrogen, and pure hydrogen at an operating temperature of 600 °C was studied. As a result, clear differences were found in the dynamics of carbon deposition depending on the exact operating parameters, such as current load applied to the cell and fuel composition. In that work, Raman spectroscopy was also used to study the removal of surface carbon from SOFC anodes using electrochemical oxidation.

In the paper [23] by the same research team, real-time monitoring of anode surfaces was performed and showed that the formation of graphitic carbon began almost immediately for anodes under open-circuit voltage. However, carbon formation was initially rapid and then stabilized, suggesting that the process was largely self-limiting under these conditions. Polarization of the anodes resulted in a significant reduction in carbon formation. In order to characterize the entire large-area surface, *ex-situ* Raman spectroscopy mapping and SEM analysis of the anode surfaces were performed. Clear changes in the carbon distribution on the anode surfaces were observed in the optical data. The change over the surfaces of polarized anodes was particularly pronounced, with distinct carbon-free regions and regions with heavy deposits. Examination of the SOFC geometry revealed that carbon was preferentially formed in the region where gas access was restricted. Computational modeling showed that regions of the anode with reduced gas access would have a much lower charge transfer current, suggesting that the blocked anode behaved similarly to an anode under OCV. As a result, carbon formation will be much more favorable in these regions, and current densities elsewhere will also be significantly altered.

An interesting feature of the work [87] by the same team is the study of solid oxide electrolysis cells (SOECs). The paper showed that charge transfer reactions occurring at the triple phase boundary (TPB) during CO_2 electrolysis promoted carbon deposition because of local changes in the gas

composition. *Ex-situ* mapping by Raman spectroscopy was used in combination with numerical modeling to show that most of the carbon was formed near the electrode/electrolyte interface during CO–CO_2 electrolysis. This represents a potential limitation of in-situ Raman spectroscopy in the study of SOECs. As a surface-sensitive technique, Raman spectroscopy does not fully reflect the interactions within the bulk of the electrode. Therefore, a better understanding of the interactions within solid oxide devices is achieved by combining in-situ and *ex-situ* Raman spectroscopy methods, as well as other analytical techniques. The results of combined *ex-situ* Raman spectroscopy and SEM analysis showed that the GDC interlayer reduced carbon deposition in Ni/GDC electrodes and improved mechanical stability under CO–CO_2 electrolysis conditions.

In the work [88] of another group of authors, both a SOEC system for carbon dioxide reduction and a SOFC system for electrical energy generation were also investigated. In that work, an interesting geometry with nickel strips was used to study carbon deposition at different locations. It was shown that for the SOFC mode, carbon deposition could be significantly enhanced by overpotential, and carbon was deposited much heavier near the TPB than in the middle of the Ni strips. In contrast, for the SOFC mode, the deposited carbon could be directly consumed by electrooxidation, and the carbon content near the TPB was lower than in the middle of the strips. The deposited carbon produced or consumed by the electrochemical reaction was mainly in the crystalline graphitic carbon structure. In [89], the measurements performed using *ex-situ* Raman spectroscopy on SOEC samples used during CO_2/CO electrolysis revealed the presence of both disordered and graphitic carbon on the surface of the nickel electrode.

Returning to the in-situ detection of carbon deposition using methane as a fuel, the work [90] must be mentioned separately. This work showed that when the cell was in the OCV mode during operation on methane, carbon began to deposit on the surface of the nickel mesh electrode. Carbon deposition was clearly recorded as a change in the reflectance on the nickel surface (simple optical microscopy), as well as by the emergence of a specific peak with a shift of about 1560 cm^{-1} in the Raman spectra; the deposited carbon was in the form of graphite. The carbon coating on the surface was non-uniform: it varied from grain to grain. When a certain overpotential was applied to the anode, carbon gradually disappeared from the edge of the electrode, i.e., from the electrode/electrolyte interface, where oxygen was electrochemically supplied. In the authors' opinion, this experiment is the first in-situ observation of the electrochemical oxidation of carbon under the real operating conditions of a SOFC.

In a much later study [91] by other authors, the same system was investigated: a solid oxide fuel cell (SOFC) fueled by methane in the form of a methane-hydrogen mixture. An interesting feature of this study is the use of cells with an optically transparent electrolyte, which enables the collection of information from the internal anode/electrolyte interface. The work was carried out using an experimental setup, which is schematically illustrated in Fig. 4.

By using flow-through gas analysis in combination with in-situ Raman spectroscopy and electrochemical techniques,

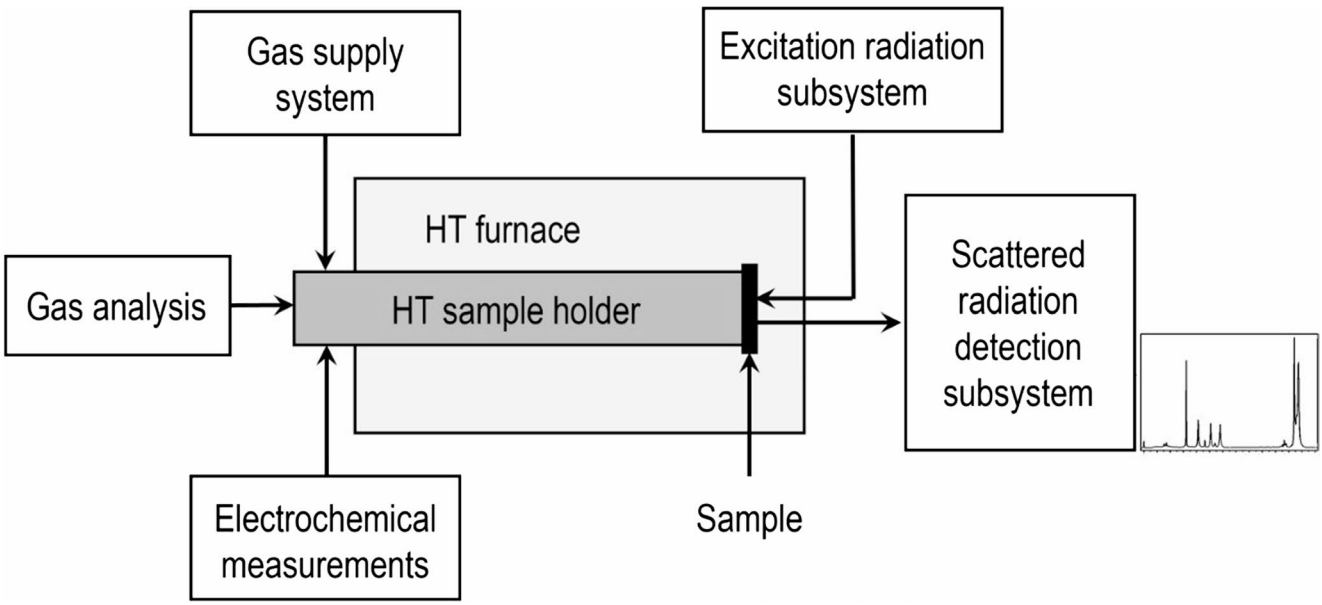

Fig. 4 Schematic illustration of the experimental setup [91] combining in-situ Raman spectroscopy, electrochemical measurements, and gas analysis

this study demonstrated that the addition of methane led to the formation of carbon monoxide and an increase in the hydrogen content in the reaction products. At the same time, the methane content in the conversion products decreased. It was shown that a more significant decrease in methane content relative to the increase in the hydrogen and CO concentrations may be associated with the Boudoir reaction and carbon deposition. This is confirmed by the fact that the electrochemical characteristics of the fuel cell deteriorated over time due to carbonization of the SOFC anode when operating on methane-rich mixtures. Model experiments examined the effect of hydrocarbon-containing fuel on the evolution of the microstructure and chemical composition of the fuel electrode. A peak of amorphous carbon was detected in the Raman spectra. It was shown that its formation was associated with carbon deposition on the model SOFC when using hydrocarbon gas mixtures as fuel. Hence, in-situ Raman spectroscopy enables the study of carbon deposition on SOFC anodes using various hydrocarbons as fuel, as well as the processes of removing these deposits using specialized gaseous agents. This technique allows for the separation of ordered (graphitic) and disordered (amorphous) carbon and enables the localization of processes across the electrode surface. By investigating carbon deposition, in-situ Raman spectroscopy also enables the study of electrooxidation mechanisms for various hydrocarbons, including quite complex ones. Additionally, it is possible to explore methods for counteracting carbon deposition and the significant role of SERS in these studies.

Assessment of the kinetics and mechanisms of SOFC anode reduction

Studying the reduction-oxidation kinetics of composite SOFC anodes is crucial for both understanding fuel oxidation mechanisms and optimizing the reduction process of electrochemical devices. Therefore, this aspect of SOFC operation is widely studied in the scientific literature [118–120]. In-situ Raman spectroscopy is also actively used to investigate the kinetics and mechanisms of SOFC anode reduction. A summary of the works in this area is provided in Table 5.

The authors of Ref. [121] developed a new experimental technique that is based on the use of SOFCs containing optically transparent single-crystal membranes made of stabilized cubic zirconia. A schematic illustration of the corresponding cell geometry is shown in Fig. 5 (top right). In contrast to the conventional geometry (top left), which only provides information from the outer boundary of the sample, the new cell geometry makes it possible to collect Raman spectra from the internal interface of the electrode and electrolyte, thus increasing informativeness of the studies. Photos of cells with the new geometry are shown in the bottom part of Fig. 5 (the cathode side is on the left and the anode side is on the right).

A new cell design and an experimental methodology combining electrochemical studies and in-situ Raman spectroscopy were tested to study the kinetics of SOFC anode reduction. The time dependencies of the intensity and area of the two-phonon peak of nickel oxide were plotted to track anode reduction.

In [122], studies using a new sample geometry and a combined in-situ technique were continued. Optical and thermogravimetric studies showed that the first reduction cycle differed significantly from subsequent cycles in both the initial delay and the overall duration of the process. Figure 6 depicts characteristic dependencies of the intensity of the selected Raman peak as a function of time for the first three reduction cycles.

SEM studies showed that these changes were associated with a fundamental morphological restructuring that occurred during the first reduction cycle: the size of the nickel oxide grains decreased significantly compared to their original size [122]. Figure 7 compares the micrographs of the composite anode before and after reduction. It is evident that the size of the nickel oxide grains decreased during the reduction process, while the grains of zirconia solid electrolyte remained visually unchanged.

In Ref. [123], a more systematic study of this system was carried out. Reliable data on the reduction of NiO were obtained, which are consistent with the kinetic parameters and microscopic mechanisms known in the literature. After initial microstructural reconstruction by redox cycling, the behavior of standard cermet anodes in a flowing H_2–N_2 atmosphere can be described by the classical Avrami model [127, 128].

Continuing the studies described above, a model for the reduction of the SOFC anode substrate of a Ni-YSZ cermet composite was developed [124]. According to this model, the reduction processes can occur in four modes depending on the temperature and flow rate of the supplied fuel: (i) uniform reduction throughout the entire volume of the sample, the reaction rate is limited by the amount of supplied hydrogen; (ii) uniform reduction throughout the entire volume of the sample, the reaction rate is limited by the kinetics of the reaction of NiO particle reduction; (iii) reduction occurs by the front, the reaction rate is limited by the kinetics of the front movement; (iv) reduction occurs by the front, the reaction rate is limited by the amount of supplied hydrogen. It was found that a high reaction rate of NiO reduction required a higher hydrogen flow per unit area of the sample for direct kinetic measurements. According to the model, the electrochemical measurements confirmed the assumptions about the movement of the front, and it was shown

Table 5 A summary of the works where studies of the kinetics of SOFC anode reduction were carried out using in-situ Raman spectroscopy

Cells and materials	Temperature, °C	Raman lines, cm^{-1}	Brief conclusion	Ref.
10Sc1YSZ – Ni/10Sc1CeSZ	600	1150, 1460	The experimental technique was based on the use of SOFC cells containing optically transparent single-crystal membranes made of stabilized cubic zirconia. Combined with electrochemical measurements, this method enabled a direct study of the redox processes in the boundary zone of the triple phase region under varying current density, temperature, and gas phase composition.	[121]
Ni/10Sc1CeSZ	500	615	Studies using Raman spectroscopy and thermogravimetric analysis methods showed that the first reduction cycle differed significantly from subsequent cycles in both the initial delay and the overall process duration.	[122]
ESC SOFC: Ni/10Sc1CeSZ − 10Sc1YSZ – LSM/10Sc1CeSZ	400–600	615, 1100	The data on NiO reduction are consistent with the kinetic parameters and microscopic mechanisms known in the literature: after initial microstructural reconstruction by redox cycling, the behavior of standard cermet anodes in a flowing H_2–N_2 atmosphere can be described by the classical Avrami model.	[123]
ASC SOFC: ACC-AF-8YSZ from KCeracell + LSCF	600	1070	A model for the reduction of the SOFC anode substrate of a Ni-YSZ cermet composite was developed. According to the model, the electrochemical measurements confirmed the assumptions regarding the movement of the front, demonstrating its constant speed. Based on the Raman spectral data, the thickness of the reduced NiO layer was calculated and was found to be in good agreement with the Ni skin depth.	[124]
YSZ - Ni/YSZ	715	1070	Exposure to H_2 led to a rapid decrease in the intensity of the NiO band (1072 cm^{-1}), i.e., a reduction to Ni. The reduction was complete within 2 min of the initial exposure to H_2. In less reducing atmospheres, the rate is slower, but the process was still complete within 10 min. Switching the gas phase back to air reoxidized Ni to NiO, and the process was again complete within a few minutes. In-situ Raman spectroscopy is sensitive enough to report the disappearance and reappearance of the NiO band and to track the kinetics of this process on a time scale of minutes.	[64]
Ni/YSZ	575	1100	The oxidation of Ni by O_2 followed first-order (or pseudo-first-order) kinetics, while Ni oxidation by water vapor exhibited linear kinetics in the early stages, which resembled zero-order kinetics. The reduction of NiO by H_2 occurred on a time scale approaching experimental resolution. Water can oxidize Ni, a reaction that is not often recognized in kinetic models developed to describe the chemistry of SOFC anode materials. The oxidation of Ni occurred via two distinct mechanisms depending on the oxidizing agent.	[125]
Ni - YSZ	715, 550	1070	Hydrogen reduction occurred within seconds; however, surface oxidation required 5–10 min to reach the asymptotic limit. The kinetics of Ni oxidation were studied for samples prepared with three different sizes of Ni particles (the cell was divided into different sectors). The initial particle size was not a significant factor in controlling pseudo-first-order oxidation rates. Furthermore, water vapor itself did not oxidize Ni particles. However, humidity affected the susceptibility of Ni to subsequent oxidation when H_2O was replaced by O_2. After exposure to water, Ni oxidation followed two separate first-order kinetic processes. This effect occurred only for the first oxidation cycle after exposure to water.	[126]

that it moved at a constant speed. The threshold value of the reduction reaction in the hydrogen deficiency mode obtained in that work is consistent with the literature data. Based on the Raman spectral data, calculations of the thickness of the reduced NiO layer were carried out, which are in good agreement with the thickness of the Ni skin layer.

In a much earlier study [64] by another group of researchers, perhaps the pioneering study of this topic was performed using in-situ Raman spectroscopy. It was shown that exposure to H_2 led to a rapid decrease in the intensity of the NiO band shifted at 1072 cm^{-1} as NiO was reduced to metallic Ni. The data indicate that the reduction of Ni was complete within two minutes of the initial exposure to H_2. In less reducing atmospheres (such as humid CH_4, 8% in Ar), the reduction rates were slower, but the process was still complete within 10 min of the initial exposure. Switching the gas phase back to air reoxidized Ni to NiO, and the process was again complete within a few minutes. These data demonstrate that in-situ Raman spectroscopy is sensitive enough to report the disappearance and reappearance of the NiO band and to monitor the kinetics of this process on a time scale of minutes, which is particularly relevant for the electrochemical processes occurring in SOFCs.

In a later study by the same authors [125], the same Ni/YSZ system was examined. It was shown that Ni oxidation by O_2 appeared to follow first-order (or pseudo-first-order) kinetics, while Ni oxidation by water vapor exhibited linear kinetics in the early stages, which resembled zero-order kinetics. The reduction of NiO by H_2 occurred on a time scale approaching experimental resolution. These results

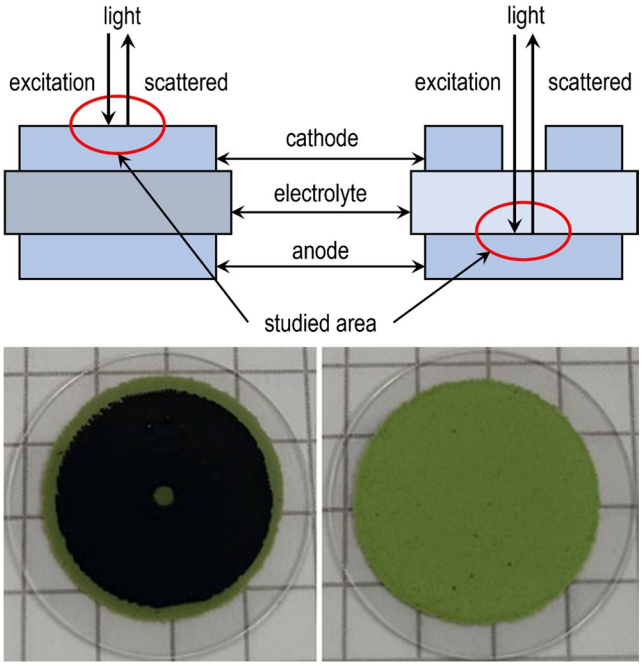

Fig. 5 Top: conventional geometry of the cells for Raman measurements (right) and alternative geometry with an optically transparent electrolyte [121] (left). Bottom: photographs of the cell with the new geometry (the cathode side is on the right and the anode side is on the left)

are significant for several reasons. First, the data clearly demonstrate that water can oxidize Ni, a reaction that is not often recognized in kinetic models developed to describe the chemistry occurring at SOFC anode materials. Second, the data imply that Ni oxidation proceeds via two different mechanisms depending on the oxidant.

For a similar system [126], the authors showed that hydrogen reduction occurred within seconds; however, surface oxidation required 5–10 min to reach the asymptotic limit. The kinetics of Ni oxidation were studied for samples prepared with three different sizes of Ni particles (5–20 nm, 2–3 μm, and 3–7 μm). The data indicate that the initial particle size is not a significant factor in controlling pseudo-first-order oxidation rates. Furthermore, in contrast to other studies, water vapor itself does not appear to oxidize Ni particles. However, humidity does affect the susceptibility of Ni to subsequent oxidation when H_2O is replaced by O_2. After exposure to water, Ni oxidation appears to follow two separate first-order kinetic processes. This effect is shown to occur only for the first oxidation cycle after exposure to water, a finding that is in excellent agreement with the results of [122].

Hence, in-situ Raman spectroscopy combined with electrochemical and structural analysis methods allows us to study the mechanisms and kinetics of SOFC anode reduction and to identify the main limiting factors depending on the operating conditions of the SOFC.

Oxygen chemical potential variations

Investigating variations in the oxygen chemical potential in the electrochemical reaction zone is crucial for understanding the mechanisms of current-generating processes [129–131]. In-situ Raman spectroscopy is actively used as a highly promising research method in this area. A summary of relevant studies is presented in Table 6.

The report [132] can be considered the pioneering work in this area. In this article, as a result of studying both the Stokes/anti-Stokes ratio and the peak shift method for determining the surface temperature and the relative changes in the surface temperature from site to site throughout the sample, it was concluded that the peak shift method was more reliable and faster and was capable of providing higher resolution. These results pave the way for the development of an in-situ method that is capable of mapping the temperature distribution with very high spatial resolution in operating SOFCs while simultaneously monitoring the chemical composition.

In Refs. [133] and [134], changes in the oxygen chemical potential on the top surface of the anode during polarization were successfully quantified using SDC as a probe at $P(O_2)$ below about 10–17 atm. The chemical potential of oxygen on the anode surface increased with an increase in the anodic overpotential up to 180 mV. This change in the chemical potential of oxygen resulted from two overpotential-dependent factors: an increase in $P(O_2)$ by electrochemically generated steam and an expansion of the electrochemically active zone.

The F_{2g} peak area of cerium dioxide sensitive to oxygen nonstoichiometry was shown to exhibit visible changes depending on the anodic current and the partial pressure of hydrogen [135]. Under isothermal conditions, the expected local overpotentials were determined exclusively by the current density. The corresponding mechanisms determining the transport rate can be associated with the transfer of ions through the GDC/YSZ interface. Subsequent steps limiting the transport rate, such as electrochemical oxidation of hydrogen in the Ni-GDC layer, were not detected in the tested anode design due to the limited penetration depth of the exciting radiation. To study these steps using in-situ Raman spectroscopy, it is necessary to form directly a three-phase boundary on the YSZ single crystal.

In Ref. [136], the dependencies of the Raman spectral line at a frequency of 460 cm^{-1} (F_{2g} CeO_2) on the applied current load were obtained for both types of cells (with a supporting anode, ASC, and an electrolyte, ESC) and for different fuel mixture compositions. Raman measurements on ASC samples showed significantly higher sensitivity and allowed for an expansion of the range of current loads (up to 2 A/cm^2) and operating temperatures (650–750 °C). The

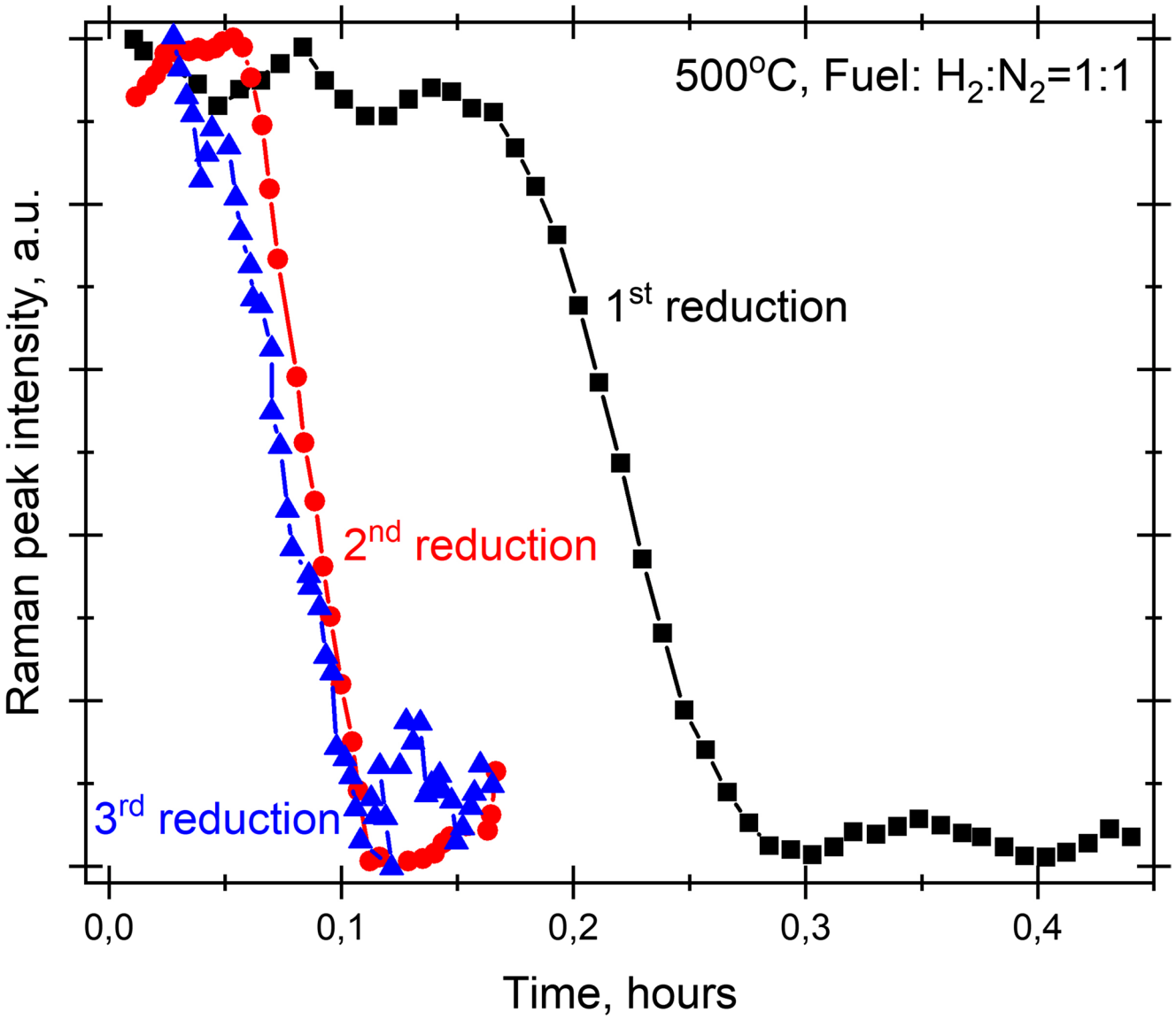

Fig. 6 Characteristic time dependencies of the studied Raman peak intensity for the first three reduction cycles [122]

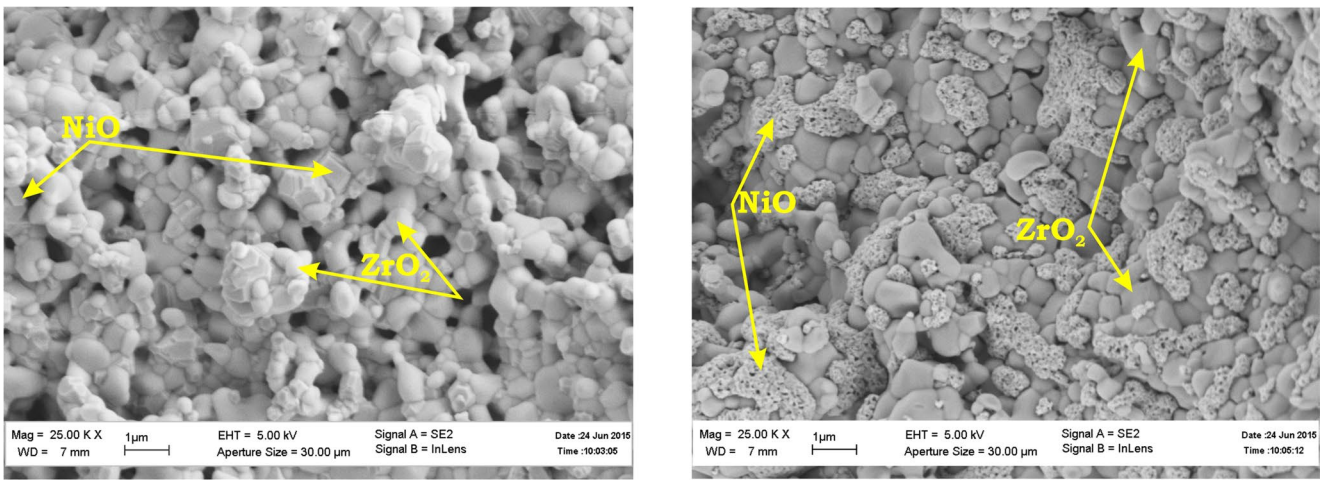

Fig. 7 Comparison of the microstructures of the composite anode before and after reduction cycles

Table 6 A summary of the works where analysis of the oxygen chemical potential was carried out

Cells and materials	Temperature, °C	Raman line, cm^{-1}	Brief conclusion	Ref.
GDC disk	600	~ 460 - F_{2g} CeO_2	The peak shift method is more reliable and faster and is capable of providing higher resolution. Work has begun on developing an in-situ method for mapping the temperature in operating SOFCs while simultaneously monitoring their chemical composition.	[132]
Ni − $Ce_{0.8}Sm_{0.2}O_{2-\delta}$	700	~ 460 – F_{2g} CeO_2 540–600 – O vacancies	The change in the chemical potential of oxygen on the upper anode surface during polarization was successfully quantified. An increase in the chemical potential on the anode surface with an increase in the anodic overpotential resulted from two overpotential-dependent factors: an increase in $P(O_2)$ by electrochemically generated steam and an expansion of the electrochemically active zone.	[133] [134]
ESC SOFC	850	~ 460 – F_{2g} CeO_2	The F_{2g} peak area of CeO_2 varied with anodic current and hydrogen partial pressure. Rate-determining mechanisms may be related to ion transport across the GDC/YSZ interface. Subsequent rate-limiting steps, such as electrochemical oxidation of hydrogen in the Ni-GDC layer, were undetectable due to the limited penetration depth of the laser beam.	[135]
ESC SOFC ASC SOFC	750	~ 460 – F_{2g} CeO_2	Dependencies of the F_{2g} CeO_2 line on the current load for ESC and ASC cells and for various fuel mixture compositions were obtained. RS measurements on ASC samples demonstrated greater sensitivity, extending the range of current loads and operating temperatures. The general shape of the dependencies was similar and could be attributed to the transport of oxygen anions from the electrolyte to the anode.	[136]
ASC SOFC	750	~ 460 – F_{2g} CeO_2	The feasibility of direct measurements at the internal "electrolyte/anode" interface in the case of a polycrystalline thin-film zirconium solid electrolyte was experimentally demonstrated using optical transparency tests and Raman studies. Oxygen anions were directly transported from the YSZ electrolyte membrane to the cerium-based anode sublayer, which supported the "oxygen spillover" mechanism.	[137]
ESC SOFC ASC SOFC	750	~ 460 – F_{2g} CeO_2	There was a linear relationship between the F_{2g} peak area of CeO_2 and the chemical potential of oxygen at the anode/electrolyte interface. At higher current loads, the overpotential dependence showed significant differences for different cell types, indicating an increased role of exchange processes with the gas phase. Combination of optical measurements with electrochemical studies made it possible to evaluate the dependence of the local anodic overpotential on the current load. The overpotential exhibited the Tafel behavior.	[138] [91]
SOFC: Pt/CGO/Pt	900 200	~ 460 – F_{2g} CeO_2 540–600 – O vacancies	Systematic doping of cerium with various lanthanides allowed the authors to correlate the Raman shift with the structural changes in the cubic fluorite cell caused by the dopant. The advantages of the Raman method for tracking in-situ temperature changes (e.g. changes in the cell volume due to purely thermal effects or effects due to the formation of oxygen vacancies) were demonstrated.	[139]
8YSZ in operating SOFCs	715	~ 600 – F_{2g} YSZ	The YSZ surface can be affected by the reducing and oxidizing atmospheres observed during standard SOFC operation. The effect was quantified by a 50% reduction in the F_{2g} peak of YSZ under reducing conditions, a phenomenon being reversible upon cycling. Near the TPB, YSZ became even more reduced as the overpotential increased. The altered electronic structure of the reduced surface layer can improve electronic conductivity. YSZ with a reduced surface can promote the propagation of chemical reactions from the electrodes, thereby effectively increasing the width of the electrochemically active region.	[140]

general shape of the dependencies is quite similar; it can be attributed to the transport of the oxygen anion from the solid electrolyte membrane to the anode electrode.

The possibility of direct measurements at the internal "electrolyte/anode" interface in the case of a polycrystalline thin-film zirconium solid electrolyte was further demonstrated experimentally using optical transparency tests and Raman spectroscopy studies [137]. Oxygen anions were directly transported from the YSZ electrolyte membrane to the cerium-based anode sublayer, which supported the "oxygen spillover" mechanism [141–143].

In Refs. [91, 138], a linear relationship between the change in the area of the peak shifted at about 460 cm^{-1} (F_{2g} CeO_2) and the level of the chemical potential of oxygen in the region of the internal "anode/electrolyte" interface was shown. The rate-limiting mechanism in the reaction zone at low current densities could be associated with the transport of anions through this interface. At higher current loads, the dependence of the overpotential showed

significant differences for different cell types, which indicates an increasing role of exchange processes with the gas phase (e.g., hydrogen oxidation on the GDC surface or near the interface between the three phases). A combination of optical measurements with electrochemical studies made it possible to evaluate the dependence of the local anodic overpotential on the current load applied to the cell. In both cases, the overpotential exhibited the Tafel behavior [144, 145]. A comparative analysis of the anodic impedance with different fuel gas mixtures suggests that spectroscopic measurements of the internal interfaces provide direct information on the contribution of the fuel oxidation reaction to the total losses of SOFCs.

Finally, a systematic study of doping of cerium oxide with various lanthanides was carried out in [139]. It allowed the shift of the Raman lines to be correlated with the structural changes in the cubic fluorite cell caused by the dopant. The study of praseodymium-doped cerium oxide at high temperatures demonstrated the advantages of the Raman method for in-situ monitoring of changes with temperature (e.g. changes in the cell volume due to purely thermal effects or effects due to the formation of oxygen vacancies), which can subsequently be related to the cell expansion and electrochemical properties.

In Ref. [140], instead of the more frequently studied doped cerium dioxide (GDC) [146, 147], a more classical electrolyte based on stabilized zirconia (YSZ) [148, 149] was studied. Initial in-situ Raman measurements showed that the YSZ surface could be affected by the reducing and oxidizing atmospheres that were realized in two gas volumes during standard SOFC operation. This effect was quantified by a 50% decrease in the intensity of the F_{2g} peak of YSZ under reducing conditions. This effect was reversible upon cycling from a reducing to an oxidizing environment. In-situ Raman spectroscopy was used to measure the relative oxide concentration on the YSZ surface. The data demonstrated that near the triple-phase boundary, YSZ became even more reduced as the overpotential increased. This observed surface reduction suggests an explanation for the observed decrease in the impedance on the YSZ surface with an increase in the cell polarization: the altered electronic structure of the reduced surface layer can slightly improve electronic conductivity. YSZ with a reduced surface can also promote the propagation of chemical reactions from the electrodes, thereby effectively increasing the width of the electrochemically active region.

Hence, in-situ Raman spectroscopy can be successfully applied to monitor the chemical potential of oxygen over a wide range of operating conditions, including partial pressure, temperature, and anodic overpotential, as well as in various materials used to create SOFCs. Optical data enable an evaluation of purely electrochemical characteristics, such as the dependence of anodic overpotential on current load.

Application of in-situ Raman spectroscopy for gas analysis

One of the promising methods for studying the mechanisms of processes occurring in SOFCs is gas analysis [150–152]. Raman spectroscopy is also used for in-situ studies of SOFCs as a tool for gas analysis. A summary of studies in this area is provided in Table 7.

For instance, Raman spectroscopy was successfully used to determine the distribution of the main gaseous substances along the flow in an optically accessible model of a DIR-SOFC reformer at operating temperatures of 600 and 700 °C [153]. A calibration methodology was developed that allows the experimental results to be presented as the mole fraction of substances.

In Refs. [154] and [155], a primary calibration was first performed. When the channel was filled with cold air, the Raman bands of N_2, O_2, and residual H_2O were well resolved. This method was then successfully applied to the diagnostics of a SOFC operating under standard conditions: 1123 K and dry hydrogen as a fuel. Under these conditions, the Raman bands of H_2 and H_2O were detected and provided a sufficient signal-to-noise ratio for quantification after accumulation. The profiles were recorded with a spatial resolution of 1 mm along the channel length and clearly demonstrated the expected behavior, i.e., a decrease in the H_2 concentration and an increase in the H_2O concentration along the flow direction. However, because of leaks in the experimental cell, the concentrations could not be quantified.

In [150], a methodology was developed for the next work by the same authors [156]. In [156], the results obtained under OCV conditions and low current densities showed possible competition between carbon dioxide and water in internal methane reforming, which led to the presence of two different types of methane reforming: steam and dry. The chemical gradient of CH_4 along the cell surface was the same under the three studied conditions, indicating that it was not affected by the current at all. The contribution of WGSR to OCV was shown only in the anode region, close to the cell outlet. This may due to the strong presence of the endothermic reforming reaction, which hides the exothermic contribution of WGSR along the surface. At the same time, under current, its contribution was apparently greater, which led to an increase in water and CO_2. Moreover, at low fuel utilization values, the authors demonstrated the readiness of SOFCs for the co-production of hydrogen along with the generation of electricity.

Table 7 A summary of works in which studies were carried out using Raman spectroscopy as a gas analysis tool

Cells and materials	Operating temperature, °C	Gases studied	Brief conclusion	Ref.
Ni/YSZ anode	600, 700	N_2, H_2, CH_4, H_2O	Raman spectroscopy was used to determine the flow distribution of key gaseous species in an optically accessible DIR-SOFC reformer at operating temperatures of 600 and 700 °C. A calibration methodology was developed that allows the results to be presented as mole fractions of the species.	[153]
SOFC: Ni/GDC – 3YSZ - LSM/8YSZ – LSM	900	O_2, N_2, H_2O	The method was successfully applied to SOFCs operating on dry H_2. The bands of H_2 and H_2O were detected and yielded a sufficient signal-to-noise ratio for quantitative assessment. The profiles were recorded with a spatial resolution of 1 mm along the channel length, showing a	[154]
50x50 mm ESC SOFC: NiO/GDC – TZ3Y – 8YSZ/ LSM - LSM		H_2, H_2O, N_2	decrease in the H_2 concentration and an increase in the H_2O concentration along the flow direction.	[155]
			A methodology for the next work (below in the table) was developed	[150]
121 cm^2 ASC SOFC: Ni/YSZ – YSZ – GDC – LSC			At low current densities and OCV, competition between CO and H_2O in internal methane reforming was possible, resulting in two distinct types of methane reforming: steam and dry. The chemical gradient of CH_4 along the cell surface was the same under the three studied conditions, indicating that it was completely unaffected by the current. The contribution of WGSR to the OCV was demonstrated only in the anode region, close to the cell outlet. At high currents, the contribution of WGSR was greater, leading to increased water and CO_2 production. Moreover, the SOFC was demonstrated to be capable of co-producing H_2 along with electricity generation at low fuel utilization rates.	[156]

Hence, in-situ Raman spectroscopy can be successfully applied as a gas analysis technique to assess the distribution of gaseous components in a fuel mixture and to determine the mechanism of fuel conversion.

Conclusions

In-situ Raman spectroscopy is an extremely convenient and informative method for solving a number of critical research problems related to the study and development of SOFCs, such as assessing mechanical stresses, SOFC anode poisoning with sulfur- and chlorine-containing compounds, carbon deposition on SOFC anodes when using various hydrocarbons as fuel, studying the mechanisms and kinetics of SOFC anode reduction, and monitoring the chemical potential of oxygen, as well application as a gas analysis technique.

When assessing mechanical stresses during SOFC operation, the accuracy of the method is in the range of tens of MPa, and both the position and half-width of peaks in the Raman spectra can be used as a source of information.

Studies of SOFC anode poisoning with sulfur-containing compounds can be carried out over extremely wide concentration ranges. When combined with more traditional electrochemical techniques, this method enables detailed investigation of degradation mechanisms, identification of various compounds formed during poisoning, and detection of their removal under specific conditions. In-situ Raman spectroscopy also enables successful studies of SOFC anode poisoning with chlorine-containing fuel impurities. It is worth noting that it is possible to study combined poisoning with chlorine and carbon deposition on the SOFC anode.

When investigating carbon deposition on the anode, this technique allows for the separation of ordered (graphitic) and disordered (amorphous) carbon and the localization of processes across the electrode surface. By studying carbon deposition, in-situ Raman spectroscopy also enables the study of the electrooxidation mechanisms of various hydrocarbons, including complex ones. Furthermore, the significant role of SERS in these studies should be noted.

When combined with electrochemical and structural analysis methods, this technique also allows studying the mechanisms and kinetics of SOFC anode reduction and identifying key limiting factors depending on the cell

operating conditions. In-situ Raman spectroscopy can be successfully used to monitor the chemical potential of oxygen over a wide range of operating conditions, as well as in various materials used to create SOFCs. Optical data allows for the evaluation of purely electrochemical characteristics. This technique can be successfully applied as a gas analysis method to assess the distribution of gaseous components in a fuel mixture and to determine the fuel conversion mechanism.

Acknowledgements The author would like to express his gratitude to Dr.S. Sergey Bredikhin and Dr. Ilya Burmistrov for the idea of the review and fruitful discussions, to Dr. Evgeny Tikhonov for the effective organization of the system of scientific sources, and to Maria Dyakina for preparing informative illustrations.

References

1. Dokiya M (2002) SOFC system and technology. Solid State Ion 152–153:383–392. https://doi.org/10.1016/S0167-2738(02)00345-4
2. Faro ML, Antonucci V, Antonucci PL, Aricò AS (2012) Fuel flexibility: a key challenge for SOFC technology. Fuel 102:554–559. https://doi.org/10.1016/j.fuel.2012.07.031
3. Corigliano O, Pagnotta L, Fragiacomo P (2022) On the technology of solid oxide fuel cell (SOFC) energy systems for stationary power generation: a review. Sustainability 14(22):15276. https://doi.org/10.3390/su142215276
4. Convion C60 fuel cell co-generation system (2023). https://convion.fi/wp-content/uploads/2023/09/Convion_C60_brochure_2023.pdf. Accessed 12 Sept 2025
5. The Bloom Energy Server 6.5 (2024). https://www.bloomenergy.com/wp-content/uploads/bloom-energy-server-datasheet-2024.pdf. Accessed 12 Sept 2025
6. Huang S, Yang C, Chen H et al (2022) Coupling impacts of SOFC operating temperature and fuel utilization on system net efficiency in natural gas hybrid SOFC/GT system. Case Stud Therm Eng 31:101868. https://doi.org/10.1016/j.csite.2022.101868
7. Development History of Latest Ene-Farm Type S (2020 Model). https://www.daigasgroup.com/en/rd/topic/1768549_56103.html. Accessed 12 Sept 2025
8. Fang Q, Blum L, Stolten D (2019) Electrochemical performance and degradation analysis of an SOFC short stack following operation of more than 100,000 hours. J Electrochem Soc 166:F1320. https://doi.org/10.1149/2.0751916jes
9. Tsipis EV, Matveev DV, Sharafutdinov AU et al (2024) Performance of SOFCs using model waste gases: A case study. Fuel 358(A):130129. https://doi.org/10.1016/j.fuel.2023.130129
10. Tsipis EV, Agarkov DA, Borisov YuA et al (2023) Waste gas utilization potential for solid oxide fuel cells: A brief review. Renew Sustain Energy Rev 188:113880. https://doi.org/10.1016/j.rser.2023.113880
11. Nehter P, Wildrath B, Bauschulte A, Leites K (2017) Diesel based SOFC demonstrator for maritime applications. ECS Trans 78:171. https://doi.org/10.1149/07801.0171ecst
12. Regulations for emissions from heavy equipment with compression-ignition (Diesel) engines. https://www.epa.gov/regulations-emissions-vehicles-and-engines/regulations-emissions-heavy-equipment-compression. Accessed 12 Sept 2025
13. Höber M, Königshofer B, Boškoski P et al (2023) Diesel operated combined heat and power SOFC system: SOFC characterization and proof of concept. J Power Sources 585:233635. https://doi.org/10.1016/j.jpowsour.2023.233635
14. Miura Y, Takemiya S, Fukuyama Y et al (2023) Improvement of the internal reforming of metal-supported SOFC at low temperatures. Int J Hydrogen Energy 48(65):25487–25498. https://doi.org/10.1016/j.ijhydene.2023.03.195
15. Akbar M, An Q, Ye Y et al (2025) 400 °C operable SOFCs based on ceria electrolyte for powering wireless sensor in internet of things. Appl Energy 378(B):124916. https://doi.org/10.1016/j.apenergy.2024.124916
16. Agrawal BK, Karimi MN (2012) Thermodynamic performance assessment of a novel waste heat based triple effect refrigeration cycle. Int J Refrig 35(6):1647–1656. https://doi.org/10.1016/j.ijrefrig.2012.05.020
17. Sasaki K, Wurth J-P, Gschwend R et al (1996) Microstructure-property relations of solid oxide fuel cell cathodes and current collectors: cathodic polarization and ohmic resistance. J Electrochem Soc 143:530. https://doi.org/10.1149/1.1836476
18. Prakash BS, Kumar SS, Aruna ST (2017) Effect of composition on the polarization and ohmic resistances of LSM/YSZ composite cathodes in solid oxide fuel cell. Bull Mater Sci 40:441–452. https://doi.org/10.1007/s12034-017-1401-5
19. Zhang J, Lenser C, Menzler NH, Guillon O (2020) Comparison of solid oxide fuel cell (SOFC) electrolyte materials for operation at 500°C. Solid State Ion 344:115138. https://doi.org/10.1016/j.ssi.2019.115138
20. Prica M, Alston T, Kendall K (1997) Mechanical and thermal properties of a 200 Tube SOFC reactor. ECS Proc 1997–40:619. https://doi.org/10.1149/199740.0619PV
21. Li X, Blinn K, Chen D, Liu M (2018) In-situ and surface-enhanced raman spectroscopy study of electrode materials in solid oxide fuel cells. Electrochem Energ Rev 1:433–459. https://doi.org/10.1007/s41918-018-0017-9
22. Yu Y, Xiao T-H, Wu Y et al (2020) Roadmap for single-molecule surface-enhanced Raman spectroscopy. Adv Photon 2(1):014002. https://doi.org/10.1117/1.AP.2.1.014002
23. Maher RC, Duboviks V, Offer GJ et al (2013) Raman spectroscopy of solid oxide fuel cells: technique overview and application to carbon deposition analysis. Fuel Cells 13(4):455–469. https://doi.org/10.1002/fuce.201200173
24. Maher RC, Offer G, Brandon NP, Cohen LF (2012) In-situ raman characterization of SOFC anodes. MRS Online Proc Library 1385:201. https://doi.org/10.1557/opl.2012.852
25. Workman J Jr (2025) A New Radiation: C.V. Raman and the dawn of quantum spectroscopy, part I. Spectroscopy 40(4):30–33. https://doi.org/10.56530/pectroscopy.yo1483v7
26. Google Scholar. https://scholar.google.com. Accessed 12 Sept 2025
27. Excessive growth in the number of scientific publications. https://www.ouvrirlascience.fr/excessive-growth-in-the-number-of-scientific-publications/. Accessed 12 Sept 2025
28. Growth rates of modern science: a latent piecewise growth curve approach to model publication numbers from established and new literature databases (2021) https://www.nature.com/articles/s41599-021-00903-w. Accessed 26 Aug 2025
29. Scientists around the world report millions of new discoveries every year − but this explosive research growth wasn't what experts predicted (2024). https://www.researchgate.net/publication/385041217_Scientists_around_the_world_report_millions_of_new_discoveries_every_year_-_but_this_explosive_research_growth_wasn't_what_experts_predicted. Accessed 26 Aug 2025
30. Elcogen website. https://elcogen.com/. Accessed 12 Sept 2025
31. SOFCMAN website. https://www.sofcman.com/. Accessed 12 Sept 2025
32. BLUEGEN website. https://bluegen.eu/en/. Accessed 12 Sept 2025

33. NEW ENERDAY website. https://new-enerday.com/. Accessed 12 Sept 2025
34. Khanafer K, Al-Masri A, Vafai K, Preethichandra P (2022) Heat up impact on thermal stresses in SOFC for mobile APU applications: thermo-structural analysis. Sustain Energy Technol Assess 52:102159. https://doi.org/10.1016/j.seta.2022.102159
35. Guo M, Ru X, Yang L et al (2022) Effects of methane steam reforming on the mechanical stability of solid oxide fuel cell stack. Appl Energy 322:119464. https://doi.org/10.1016/j.apenergy.2022.119464
36. Zhou R, Cai W, Sun K et al (2025) Analysis of assembly and thermal stress in kW scaled SOFC stacks. Int Commun Heat Mass Transf 163:108702. https://doi.org/10.1016/j.icheatmasstransfer.2025.108702
37. Nagai M, Iguchi F, Onodera S et al (2011) Evaluation of stress conditions in operated anode supported type cells based on in-situ Raman scattering spectroscopy. ECS Trans 35:519–525. https://doi.org/10.1149/1.3570028
38. Iguchi F, Onodera S, Sata N, Yugami H (2012) Study of Raman peak shift under applied isostatic pressure in rare-earth-doped ceria for evaluation of quantitative stress conditions in SOFCs. Solid State Ionics 225:99–103. https://doi.org/10.1016/j.ssi.2012.06.022
39. Onodera S, Nagai M, Iguchi F et al (2013) Evaluation of stress condition of operated anode supported-type SOFC under operating conditions based on Raman scattering spectroscopy. ECS Trans 50:83–88. https://doi.org/10.1149/05048.0083ecst
40. Onuki S, Onodera S, Iguchi F et al (2013) Evaluation of stress condition of operated anode supported-type SOFC under operating conditions based on Raman scattering spectroscopy. ECS Trans 57:951–957. https://doi.org/10.1149/05701.0951ecst
41. Iguchi F, Onuki S, Shimizu M et al (2017) Application of in-situ Raman scattering spectroscopy for stress condition measurement in solid oxide fuel cells. J Ceram Soc Japan 125:213–217. https://doi.org/10.2109/jcersj2.16275
42. Malzbender J, Steinbrech RW, Singheiser L (2009) A review of advanced techniques for characterising SOFC behaviour. Fuel Cells 9:785–793. https://doi.org/10.1002/fuce.200800110
43. Oshima K, Komaya T, Yashiro K et al (2021) Comparison of residual stress measurement methods in solid oxide fuel cell. ECS Trans 103:1251–1260. https://doi.org/10.1149/10301.1251ecst
44. Hong J, Anisur MR, Heo SJ et al (2021) Sulfur poisoning and performance recovery of SOFC air electrodes. Front Energy Res 9:643431. https://doi.org/10.3389/fenrg.2021.643431
45. Kim JH, Liu M, Chen Y et al (2021) Understanding the Impact of Sulfur Poisoning on the Methane-Reforming Activity of a Solid Oxide Fuel Cell Anode. ACS Catal 11:13556–13566. https://doi.org/10.1021/acscatal.1c02470
46. Li X, Fan J, Wang Y et al (2025) Diagnostic study of sulfur poisoning in solid oxide fuel cell anodes based on total harmonic distortion analysis. J Power Sources 639:236638. https://doi.org/10.1016/j.jpowsour.2025.236638
47. Brightman EJ, Maher R, Ivey DG et al (2011) In-situ measurement of SOFC anode surface processes. ECS Trans 35:1407–1419. https://doi.org/10.1149/1.3570127
48. Lee HS, Lee HM, Park J-Y, Lim H-T (2018) Degradation behavior of Ni-YSZ anode-supported solid oxide fuel cell (SOFC) as a function of H2S concentration. Int J Hydrog Energy 43:22511–22518. https://doi.org/10.1016/j.ijhydene.2018.09.189
49. Cheng Z, Liu M (2007) Characterization of sulfur poisoning of Ni–YSZ anodes for solid oxide fuel cells using in-situ Raman microspectroscopy. Solid State Ionics 178:925–935. https://doi.org/10.1016/j.ssi.2007.04.004
50. Dong J, Cheng Z, Zha S, Liu M (2006) Identification of nickel sulfides on Ni–YSZ cermet exposed to H2 fuel containing H2S using Raman spectroscopy. J Power Sources 156:461–465. https://doi.org/10.1016/j.jpowsour.2005.06.016
51. Kim JH, Chern Z-Y, Yoo S et al (2020) Unraveling the mechanism of water-mediated sulfur tolerance via operando surface-enhanced raman spectroscopy. ACS Appl Mater Interfaces 12:2370–2379. https://doi.org/10.1021/acsami.9b17294
52. Mai Thi HH, Rosman N, Sergent N, Pagnier T (2017) Impedance and Raman spectroscopy study of effect of H_2S on Ni-YSZ SOFC anodes. Fuel Cells 17:367–377. https://doi.org/10.1002/fuce.201600182
53. Mai Thi HH, Sergent N, Pagnier T (2013) Effect of H2S on Ni-YSZ SOFC anodes: a combined in-situ Raman spectroscopy-impedance spectroscopy study. ECS Trans 58:21–36. https://doi.org/10.1149/05803.0021ecst
54. Mai Thi HH, Saubat B, Sergent N, Pagnier T (2015) In-situ Raman and optical characterization of H_2S reaction with Ni-based anodes for SOFCs. Solid State Ionics 272:84–90. https://doi.org/10.1016/j.ssi.2015.01.007
55. Jeanmonod G, Diethelm S, Van Herle J (2021) Poisoning effects of chlorine on a solid oxide cell operated in co-electrolysis. J Power Sources 506:230247. https://doi.org/10.1016/j.jpowsour.2021.230247
56. Tabish AN, Patel HC, Mani A et al (2022) Effect of H_2S and HCl contaminants on nickel and ceria pattern anode solid oxide fuel cells. Electrochim Acta 423:140592. https://doi.org/10.1016/j.electacta.2022.140592
57. Liu B, Yildiz B (2023) Computational modeling for Cr and S poisoning pathways on La0.6 Sr0.4 Co0.2 Fe0.8 O3 surfaces. ECS Trans 111:743–751. https://doi.org/10.1149/11106.0743ecst
58. Reeping KW, Walker RA (2015) In operando vibrational raman studies of chlorine contamination in solid oxide fuel cells. J Electrochem Soc 162:F1310–F1315. https://doi.org/10.1149/2.0191512jes
59. Reeping KW, Kirtley JD, Bohn JM et al (2017) Chlorine-induced degradation in solid oxide fuel cells identified by operando optical methods. J Phys Chem C 121:2588–2596. https://doi.org/10.1021/acs.jpcc.6b11548
60. Kirtley JD, Tsoi S, Qadri SN et al (2017) In-situ optical investigations of contaminants in operating solid oxide fuel cells. ECS Trans 78:1261–1272. https://doi.org/10.1149/07801.1261ecst
61. Sciazko A, Komatsu Y, Nakamura A et al (2023) 3D microstructures of solid oxide fuel cell Ni-YSZ anodes with carbon deposition. Chem Eng J 460:141680. https://doi.org/10.1016/j.cej.2023.141680
62. Cui D, Kato R, Komatsu Y et al (2025) Microstructure evolution of SOFC pure Ni anode with carbon deposition under polarization. Chem Eng J 511:161875. https://doi.org/10.1016/j.cej.2025.161875
63. Zhu P, Yao J, Wu Z et al (2022) Construction of a transient multiphysics model of solid oxide fuel cell fed by biomass syngas considering the carbon deposition and temperature effect. Chem Eng J 442:136159. https://doi.org/10.1016/j.cej.2022.136159
64. Pomfret MB, Owrutsky JC, Walker RA (2006) High-temperature raman spectroscopy of solid oxide fuel cell materials and processes. J Phys Chem B 110:17305–17308. https://doi.org/10.1021/jp0639521
65. Pomfret MB, Owrutsky JC, Walker RA (2007) In-situ studies of fuel oxidation in solid oxide fuel cells. Anal Chem 79:2367–2372. https://doi.org/10.1021/ac062189o
66. Pomfret MB, Owrutsky J, Walker R (2008) A mechanistic understanding of solid oxide fuel cell chemistry through in-situ raman spectroscopy. ECS Trans 11:99–109. https://doi.org/10.1149/1.2939080
67. Pomfret MB, Marda J, Jackson GS et al (2008) Hydrocarbon fuels in solid oxide fuel cells: in-situ Raman studies of graphite

formation and oxidation. J Phys Chem C 112:5232–5240. https://doi.org/10.1021/jp711312p
68. Eigenbrodt BC, Pomfret MB, Steinhurst DA et al (2011) Direct, in-situ optical studies of Ni−YSZ anodes in solid oxide fuel cells operating with methanol and methane. J Phys Chem C 115:2895–2903. https://doi.org/10.1021/jp109292r
69. Eigenbrodt B, Kirtley J, Walker RA (2011) In-situ optical studies of solid oxide fuel cells operating with dry and humidified oxygenated fuels. ECS Trans 35:2789–2798. https://doi.org/10.1149/1.3570278
70. Kirtley JD, Halat DM, McIntyre MD et al (2012) High-temperature "spectrochronopotentiometry": correlating electrochemical performance with in-situ Raman spectroscopy in solid oxide fuel cells. Anal Chem 84:9745–9753. https://doi.org/10.1021/ac301504g
71. Kirtley J, Singh A, Halat D et al (2013) In-situ raman studies of carbon removal from high temperature Ni–YSZ cermet anodes by gas phase reforming agents. J Phys Chem C 117:25908–25916. https://doi.org/10.1021/jp408192e
72. Kirtley JD, McIntyre MD, Halat DM, Walker RA (2013) (Invited) insights into SOFC Ni/YSZ anode degradation using in-situ spectrochronopotentiometrys. ECS Trans 50:3–15. https://doi.org/10.1149/05044.0003ecst
73. McIntyre MD, Kirtley JD, Halat DM et al (2013) In-situ spectroscopic studies of carbon formation in SOFCs operating with syn-gas. ECS Trans 57:1267–1275. https://doi.org/10.1149/05701.1267ecst
74. Kirtley JD, Steinhurst DA, Owrutsky JC et al (2014) In-situ optical studies of methane and simulated biogas oxidation on high temperature solid oxide fuel cell anodes. Phys Chem Chem Phys 16:227–236. https://doi.org/10.1039/C3CP53278J
75. Kirtley JD, Pomfret MB, Steinhurst DA et al (2015) Toward a working mechanism of fuel oxidation in SOFCs: in-situ optical studies of simulated biogas and methane. J Phys Chem C 119:12781–12791. https://doi.org/10.1021/jp511304x
76. Kirtley JD, Pomfret MB, Steinhurst DA et al (2015) In operando optical studies of SOFCs operating with butanol. ECS Trans 68:1091–1102. https://doi.org/10.1149/06801.1091ecst
77. McIntyre MD, Kirtley JD, Singh A et al (2015) Comparing in-situ carbon tolerances of Sn-infiltrated and BaO-infiltrated Ni-YSZ cermet anodes in solid oxide fuel cells exposed to methane. J Phys Chem C 119:7637–7647. https://doi.org/10.1021/acs.jpcc.5b01345
78. Drasbæk DB, Traulsen ML, Walker RA, Holtappels P (2019) Testing novel nickel and cobalt infiltrated STN anodes for carbon tolerance using in-situ Raman spectroscopy and electrochemical impedance spectroscopy. Fuel Cells 19:484–493. https://doi.org/10.1002/fuce.201800193
79. Drasbæk DB, Welander MM, Traulsen ML et al (2022) Operando characterization of metallic and bimetallic electrocatalysts for SOFC fuel electrodes operating under internal methane reforming conditions. J Mater Chem A 10:5550–5560. https://doi.org/10.1039/D1TA07299D
80. Maza WA, Steinhurst DA, McIntyre MD et al (2021) Operando optical studies of solid oxide fuel cells operating on CO and simulated syngas fuels. J Power Sources 492:229598. https://doi.org/10.1016/j.jpowsour.2021.229598
81. Blinn KS, Abernathy H, Li X et al (2012) Raman spectroscopic monitoring of carbon deposition on hydrocarbon-fed solid oxide fuel cell anodes. Energy Environ Sci 5:7913. https://doi.org/10.1039/c2ee21499g
82. Li X, Lee J-P, Blinn KS et al (2014) High-temperature surface enhanced Raman spectroscopy for in-situ study of solid oxide fuel cell materials. Energy Environ Sci 7:306–310. https://doi.org/10.1039/C3EE42462F
83. Li X, Liu M, Lee J et al (2015) An operando surface enhanced Raman spectroscopy (SERS) study of carbon deposition on SOFC anodes. Phys Chem Chem Phys 17:21112–21119. https://doi.org/10.1039/C4CP05176A
84. Li X, Liu M, Lai SY et al (2015) In-situ probing of the mechanisms of coking resistance on catalyst-modified anodes for solid oxide fuel cells. Chem Mater 27:822–828. https://doi.org/10.1021/cm503852v
85. Nagasawa T, Chen D, Lai SY et al (2016) In-situ raman spectroscopic analysis of the coking resistance mechanism on SrZr0.95Y0.05O3−x surface for solid oxide fuel cell anodes. J Power Sources 324:282–287. https://doi.org/10.1016/j.jpowsour.2016.05.079
86. Maher RC, Duboviks V, Offer G et al (2013) In-operando raman characterization of carbon deposition on SOFC anodes. ECS Trans 57:1619–1626. https://doi.org/10.1149/05701.1619ecst
87. Duboviks V, Maher RC, Kishimoto M et al (2014) A Raman spectroscopic study of the carbon deposition mechanism on Ni/CGO electrodes during CO/CO2 electrolysis. Phys Chem Chem Phys 16:13063–13068. https://doi.org/10.1039/C4CP01503G
88. Li W, Shi Y, Luo Y et al (2015) Carbon deposition on patterned nickel/yttria stabilized zirconia electrodes for solid oxide fuel cell/solid oxide electrolysis cell modes. J Power Sources 276:26–31. https://doi.org/10.1016/j.jpowsour.2014.11.106
89. Manerova J, Call AV, Sinclair DC, Elder RH (2015) Methodology for analysis of solid oxide cells via raman spectroscopy. ECS Trans 68:2083–2092. https://doi.org/10.1149/06801.2083ecst
90. Kawada T, Yashiro K, Taura T et al (2004) Microscopic observations of SOFC anodes under operation with hydrocarbon fuels. In: 2nd International Conference on Fuel Cell Science, Engineering and Technology. ASMEDC, Rochester, New York, USA, pp 53–59
91. Korableva G, Agarkov DA, Burmistrov IN et al (2021) Application of high-temperature Raman spectroscopy (RS) for studies of electrochemical processes in solid oxide fuel cells (SOFCs) and functional properties of their components. ECS Trans 103:1301–1317. https://doi.org/10.1149/10301.1301ecst
92. Cuesta A, Dhamelincourt P, Laureyns J et al (1994) Raman microprobe studies on carbon materials. Carbon 32:1523–1532. https://doi.org/10.1016/0008-6223(94)90148-1
93. Wang Y, Alsmeyer DC, McCreery RL (1990) Raman spectroscopy of carbon materials: structural basis of observed spectra. Chem Mater 2:557–563. https://doi.org/10.1021/cm00011a018
94. Dietz RE, Brinkman WF, Meixner AE, Guggenheim HJ (1971) Raman scattering by four magnons in NiO and KNi F 3. Phys Rev Lett 27:814–817. https://doi.org/10.1103/PhysRevLett.27.814
95. Hall DS, Lockwood DJ, Poirier S et al (2012) Raman and infrared spectroscopy of α and β phases of thin nickel hydroxide films electrochemically formed on nickel. J Phys Chem A 116:6771–6784. https://doi.org/10.1021/jp303546r
96. Karmazyn AD, Fiorin V, King DA (2004) Direct sticking and differential adsorption heats as probes of structural transitions: O2 on the stepped Ni{211} surface. J Am Chem Soc 126:14273–14277. https://doi.org/10.1021/ja047165i
97. Bengaard HS, Nørskov JK, Sehested J et al (2002) Steam reforming and graphite formation on Ni catalysts. J Catal 209:365–384. https://doi.org/10.1006/jcat.2002.3579
98. Wang W, Cao Y (2010) Hydrogen-rich gas production for solid oxide fuel cell (SOFC) via partial oxidation of butanol: thermodynamic analysis. Int J Hydrog Energy 35:13280–13289. https://doi.org/10.1016/j.ijhydene.2010.09.031
99. Sasaki K, Watanabe K, Teraoka Y (2004) Direct-alcohol SOFCs: current-voltage characteristics and fuel gas compositions. J Electrochem Soc 151:A965. https://doi.org/10.1149/1.1756884
100. Patel R, Patel S, Rabari D (2024) Feasibility analysis of Calooping sorption enhanced steam reforming of bio-butanol for

SOFC application: comparative study with steam and auto-thermal reforming. Energy Sources Part A Recover Util Environ Eff 46:8398–8416. https://doi.org/10.1080/15567036.2020.1765900
101. Ramos T, Veltzé S, Sudireddy BR et al (2014) Effect of Ru/CGO versus Ni/CGO co-infiltration on the performance and stability of STN-based SOFCs. Fuel Cells 14:1062–1065. https://doi.org/10.1002/fuce.201400013
102. Hussain AM, Høgh JVT, Zhang W, Bonanos N (2012) Efficient ceramic anodes infiltrated with binary and ternary electrocatalysts for SOFCs operating at low temperatures. J Power Sources 216:308–313. https://doi.org/10.1016/j.jpowsour.2012.05.036
103. Blennow P, Sudireddy BR, Persson ÅH et al (2013) Infiltrated SrTiO3:FeCr-based anodes for metal-supported SOFC. Fuel Cells 13:494–505. https://doi.org/10.1002/fuce.201200176
104. Song J, Yang C, Hu H et al (2013) Penetration depth at various Raman excitation wavelengths and stress model for Raman spectrum in biaxially-strained Si. Sci China Phys Mech Astron 56:2065–2070. https://doi.org/10.1007/s11433-013-5205-3
105. Wenzel T, Carvajal Berrio DA, Daum R et al (2019) Molecular effects and tissue penetration depth of physical plasma in human mucosa analyzed by contact- and marker-independent Raman microspectroscopy. ACS Appl Mater Interfaces 11:42885–42895. https://doi.org/10.1021/acsami.9b13221
106. Ashtikar M, Matthäus C, Schmitt M et al (2013) Non-invasive depth profile imaging of the stratum corneum using confocal raman microscopy: first insights into the method. Eur J Pharm Sci 50:601–608. https://doi.org/10.1016/j.ejps.2013.05.030
107. Li X, Blinn K, Fang Y et al (2012) Application of surface enhanced Raman spectroscopy to the study of SOFC electrode surfaces. Phys Chem Chem Phys 14:5919. https://doi.org/10.1039/c2cp40091j
108. Li X, Lee J-P, Blinn KS et al (2013) Raman spectroscopy study of SOFC electrode surfaces. ECS Trans 57:1437–1444. https://doi.org/10.1149/05701.1437ecst
109. Sharma B, Frontiera RR, Henry A-I et al (2012) SERS: materials, applications, and the future. Mater Today 15:16–25. https://doi.org/10.1016/S1369-7021(12)70017-2
110. Cialla D, März A, Böhme R et al (2012) Surface-enhanced raman spectroscopy (SERS): progress and trends. Anal Bioanal Chem 403:27–54. https://doi.org/10.1007/s00216-011-5631-x
111. Kneipp K, Moskovits M, Kneipp H (2006) Surface-enhanced Raman scattering. Springer, Berlin Heidelberg
112. Mao S, Pei F, Feng S et al (2023) Detection of trace Rhodamine B using stable, uniformity, and reusable SERS substrate based on Ag@SiO2-Au nanoparticles. Colloids Surf, A 657:130595. https://doi.org/10.1016/j.colsurfa.2022.130595
113. Zhang M, Meng L, Kalyinur K et al (2024) Fabrication and application of Ag@SiO2/Au core-shell SERS composite in detecting Cu2+ in water environment. Molecules 29:1503. https://doi.org/10.3390/molecules29071503
114. Kong X, Yu Q, Zhang X et al (2012) Synthesis and application of surface enhanced raman scattering (SERS) tags of Ag@SiO2 core/shell nanoparticles in protein detection. J Mater Chem 22:7767. https://doi.org/10.1039/c2jm16397g
115. Jin Y, Yasutake H, Yamahara K, Ihara M (2010) Improved electrochemical properties of Ni/YSZ anodes infiltrated by proton conductor SZY in solid oxide fuel cells with dry methane fuel: dependence on amount of SZY. Chem Eng Sci 65:597–602. https://doi.org/10.1016/j.ces.2009.06.033
116. Khaliullina A, Dunyushkina L, Pankratov A (2020) Transport properties of film and bulk Sr0.98Zr0.95Y0.05O3−δ membranes. Appl Sci 10:2229. https://doi.org/10.3390/app10072229
117. Nagasawa T, Hanamura K (2015) Power generation characteristics of a SOFC with a Ni/YSZ anode incorporating a SrZr0.95Y0.05O3-α proton conductor. JTST 10:JTST0011. https://doi.org/10.1299/jtst.2015jtst0011
118. Ishibashi Y, Matsumoto K, Futamura S et al (2020) Improved redox cycling durability in alternative Ni alloy-based SOFC anodes. J Electrochem Soc 167:124517. https://doi.org/10.1149/1945-7111/abac87
119. Wang X, Zhang Y, Zhang H et al (2024) Mechanism analysis of the reduction process of the NiO-YSZ anode of a solid oxide fuel cell by hydrogen. J Electrochem Soc 171:094501. https://doi.org/10.1149/1945-7111/ad6bc2
120. Hussain AM, Huang Y-L, Pan K-J et al (2020) A redox-robust ceramic anode-supported low-temperature solid oxide fuel cell. ACS Appl Mater Interfaces 12:18526–18532. https://doi.org/10.1021/acsami.0c01611
121. Agarkov D, Burmistrov I, Tsybrov F et al (2015) Analysis of interfacial processes at the SOFC electrodes by I n-situ Raman spectroscopy. ECS Trans 68:2093–2103. https://doi.org/10.1149/06801.2093ecst
122. Agarkov DA, Burmistrov IN, Tsybrov FM et al (2016) Kinetics of NiO reduction and morphological changes in composite anodes of solid oxide fuel cells: estimate using Raman scattering technique. Russ J Electrochem 52:600–605. https://doi.org/10.1134/S1023193516070028
123. Agarkov DA, Burmistrov IN, Tsybrov FM et al (2017) In-situ Raman spectroscopy analysis of the interfaces between Ni-based SOFC anodes and stabilized zirconia electrolyte. Solid State Ionics 302:133–137. https://doi.org/10.1016/j.ssi.2016.12.034
124. Sharafutdinov AU, Agarkov DA, Burmistrov IN et al (2024) Reduction kinetics of nickel-based supporting anode composite substrates under operating conditions of intermediate-temperature solid oxide fuel cells. J Solid State Electrochem 28:1987–1996. https://doi.org/10.1007/s10008-023-05458-1
125. Eigenbrodt B, Kirtley J, Walker R (2010) In-situ optical studies of reduction/oxidation kinetics in solid oxide fuel cells. Meet Abstr MA2010-02:1141–1141. https://doi.org/10.1149/MA2010-02/12/1141
126. Kirtley J, Eigenbrodt B, Walker R (2011) In-situ optical studies of oxidation kinetics of Ni/YSZ cermet anodes. ECS Trans 33:25–37. https://doi.org/10.1149/1.3589182
127. Richardson J (2003) X-ray diffraction study of nickel oxide reduction by hydrogen. Appl Catal A: Gen 246:137–150. https://doi.org/10.1016/S0926-860X(02)00669-5
128. Hulbert SF (1969) Models for solid-state reactions in powdered compacts: a review. J Brit Ceram Soc 6(1):11–20
129. Lim D-K, Im H-N, Song S-J (2016) Spatial distribution of oxygen chemical potential under potential gradients and theoretical maximum power density with 8YSZ electrolyte. Sci Rep 6:18804. https://doi.org/10.1038/srep18804
130. Zhang L, Zhu L, Virkar AV (2019) Modeling of oxygen chemical potential distribution in solid oxide electrolyzer cells. J Electrochem Soc 166:F1275–F1283. https://doi.org/10.1149/2.0121916jes
131. Berger C, Bucher E, Gspan C, Sitte W (2019) Crystal structure, oxygen nonstoichiometry, and mass and charge transport properties of the Sr-free SOFC/SOEC air electrode material La0.75Ca0.25FeO3-δ. J Solid State Chem 273:92–100. https://doi.org/10.1016/j.jssc.2019.02.032
132. Maher RC, Cohen LF, Lohsoontorn P et al (2008) Raman spectroscopy as a probe of temperature and oxidation state for gadolinium-doped ceria used in solid oxide fuel cells. J Phys Chem A 112:1497–1501. https://doi.org/10.1021/jp076361j
133. Matsui T, Eguchi K, Furukawa T et al (2015) In-operando raman spectroscopy study on oxygen chemical potential gradient in Ni-SDC cermet anode for SOFCs. ECS Trans 68:1083–1090. https://doi.org/10.1149/06801.1083ecst
134. Matsui T, Eguchi K, Furukawa T et al (2016) In operando raman spectroscopy study on oxygen chemical potential change in

Ni–SDC cermet anode for solid oxide fuel cells. J Electrochem Soc 163:F1146–F1150. https://doi.org/10.1149/2.0391610jes
135. Agarkov DA, Burmistrov IN, Tsybrov FM et al (2018) In-situ raman spectroscopy analysis of the interface between ceria-containing SOFC anode and stabilized zirconia electrolyte. Solid State Ionics 319:125–129. https://doi.org/10.1016/j.ssi.2018.02.006
136. Eliseeva G, Agarkov DA, Burmistrov I et al (2019) Raman spectra studies of inner "Anode | Electrolyte" Interface on ESC and ASC SOFCs. ECS Trans 91:457–469. https://doi.org/10.1149/09101.0457ecst
137. Eliseeva GM, Burmistrov IN, Agarkov DA et al (2020) In-situ Raman spectroscopy studies of oxygen spillover at solid oxide fuel cell anodes. Chem Prob 1(18):9–19. https://doi.org/10.32737/2221-8688-2020-1-9-19
138. Agarkov DA, Burmistrov IN, Eliseeva GM et al (2020) Comparison of in-situ Raman studies of SOFC with thick single-crystal and thin-film magnetron sputtered membranes. Solid State Ionics 344:115091. https://doi.org/10.1016/j.ssi.2019.115091
139. Solís C, Balaguer M, Serra JM (2020) In-situ Raman characterization of SOFC materials in operational conditions: a doped Ceria study. Membranes 10:148. https://doi.org/10.3390/membranes10070148
140. Eigenbrodt BC, Walker RA (2011) High temperature mapping of surface electrolyte oxide concentration in solid oxide fuel cells with vibrational Raman spectroscopy. Anal Methods 3:1478. https://doi.org/10.1039/c0ay00644k
141. Fu Z, Wang M, Zuo P et al (2014) Importance of oxygen spillover for fuel oxidation on Ni/YSZ anodes in solid oxide fuel cells. Phys Chem Chem Phys 16:8536. https://doi.org/10.1039/c3cp55076a
142. Rossmeisl J, Bessler WG (2008) Trends in catalytic activity for SOFC anode materials. Solid State Ionics 178:1694–1700. https://doi.org/10.1016/j.ssi.2007.10.016
143. Ong K, Hanna J, Ghoniem AF (2017) Investigation of a combined hydrogen and oxygen spillover mechanism for syngas electro-oxidation on Ni/YSZ. J Electrochem Soc 164:F32–F45. https://doi.org/10.1149/2.0161702jes
144. Kulikovsky AA (2009) A model for SOFC anode performance. Electrochim Acta 54:6686–6695. https://doi.org/10.1016/j.electacta.2009.06.054
145. Razmi AR, Sharifi S, Vafaeenezhad S et al (2024) Modeling and microstructural study of anode-supported solid oxide fuel cells: experimental and thermodynamic analyses. Int J Hydrog Energy 54:613–634. https://doi.org/10.1016/j.ijhydene.2023.08.296
146. Leng Y, Chan S, Jiang S, Khor K (2004) Low-temperature SOFC with thin film GDC electrolyte prepared in-situ by solid-state reaction. Solid State Ionics 170:9–15. https://doi.org/10.1016/j.ssi.2004.02.026
147. Arabacı A, Öksüzömer MF (2012) Preparation and characterization of 10mol% Gd doped CeO2 (GDC) electrolyte for SOFC applications. Ceram Int 38:6509–6515. https://doi.org/10.1016/j.ceramint.2012.05.030
148. Han M, Tang X, Yin H, Peng S (2007) Fabrication, microstructure and properties of a YSZ electrolyte for SOFCs. J Power Sources 165:757–763. https://doi.org/10.1016/j.jpowsour.2006.11.054
149. Chen Y-Y, Wei W-CJ (2006) Processing and characterization of ultra-thin yttria-stabilized zirconia (YSZ) electrolytic films for SOFC. Solid State Ionics 177:351–357. https://doi.org/10.1016/j.ssi.2005.10.010
150. Pumiglia D, Santoni F, Viceconti E et al (2017) SOFC anode process characterization by means of a spot-sampling set-up for in-operando gas analysis. ECS Trans 75:1–8. https://doi.org/10.1149/07549.0001ecst
151. Roberson CJ, Schafer D, Roberts RA (2025) Integration of residual gas analysis mass spectrometry into a solid oxide fuel cell test stand for emissions characterization. In: AIAA Aviation Forum and Aascend 2025. American Institute of Aeronautics and Astronautics, Las Vegas
152. Papurello D, Borchiellini R, Bareschino P et al (2014) Performance of a solid oxide fuel cell short-stack with biogas feeding. Appl Energy 125:254–263. https://doi.org/10.1016/j.apenergy.2014.03.040
153. Saunders JEA, Davy MH (2012) High-temperature vibrational Raman spectroscopy of gaseous species for solid-oxide fuel cell research. Int J Hydrog Energy 37:3403–3414. https://doi.org/10.1016/j.ijhydene.2011.11.044
154. Schiller G, Auer C, Bessler WG et al (2013) A novel concept for in-situ gas-phase laser Raman spectroscopy for solid oxide fuel cell research. Appl Phys B 111:29–38. https://doi.org/10.1007/s00340-012-5303-3
155. Schiller G, Auer C, Ilhan Z et al (2013) A novel concept for in-situ gas-phase laser Raman spectroscopy for SOFC. ECS Trans 57:1339–1348. https://doi.org/10.1149/05701.1339ecst
156. Santoni F, Silva Mosqueda DM, Pumiglia D et al (2017) In-situ study of the gas-phase composition and temperature of an intermediate-temperature solid oxide fuel cell anode surface fed by reformate natural gas. J Power Sources 370:36–44. https://doi.org/10.1016/j.jpowsour.2017.09.078